Chemical Engineering Journal 430 (2022) 132761

Contents lists available at ScienceDirect

Chemical Engineering Journal

journal homepage: www.elsevier.com/locate/cej

Predicting the effects of environmental parameters on the spatio-temporal distribution of the droplets carrying coronavirus in public transport – A machine learning approach

Mehrdad Mesgarpour [a], Javad Mohebbi Najm Abad [b], Rasool Alizadeh [c], Somchai Wongwises [a,d], Mohammad Hossein Doranehgard [e], Saeed Jowkar [f], Nader Karimi [g,h,*]

[a] Fluid Mechanics, Thermal Engineering and Multiphase Flow Research Lab. (FUTURE), Department of Mechanical Engineering, Faculty of Engineering, King Mongkut's University of Technology Thonburi (KMUTT), Bangmod, Bangkok 10140, Thailand
[b] Department of Computer Engineering, Quchan Branch, Islamic Azad University, Quchan, Iran
[c] Department of Mechanical Engineering, Quchan Branch, Islamic Azad University, Quchan, Iran
[d] National Science and Technology Development Agency (NSTDA), Pathum Thani 12120, Thailand
[e] Department of Civil and Environmental Engineering, School of Mining and Petroleum Engineering, University of Alberta, Edmonton, Alberta T6G 1H9, Canada
[f] Aerospace Engineering Department, Sharif University of Technology 14588-89694, Iran
[g] School of Engineering and Materials Science, Queen Mary University of London, London E1 4NS, United Kingdom
[h] James Watt School of Engineering, University of Glasgow, Glasgow G12 8QQ, United Kingdom

ARTICLE INFO

Keywords:
COVID-19
Droplets distribution
Droplet Suspension
Machine learning
Computational Fluid Dynamics
Prediction Models

ABSTRACT

Human-generated droplets constitute the main route for the transmission of coronavirus. However, the details of such transmission in enclosed environments are yet to be understood. This is because geometrical and environmental parameters can immensely complicate the problem and turn the conventional analyses inefficient. As a remedy, this work develops a predictive tool based on computational fluid dynamics and machine learning to examine the distribution of sneezing droplets in realistic configurations. The time-dependent effects of environmental parameters, including temperature, humidity and ventilation rate, upon the droplets with diameters between 1 and 250μm are investigated inside a bus. It is shown that humidity can profoundly affect the droplets distribution, such that 10% increase in relative humidity results in 30% increase in the droplets density at the farthest point from a sneezing passenger. Further, ventilation process is found to feature dual effects on the droplets distribution. Simple increases in the ventilation rate may accelerate the droplets transmission. However, carefully tailored injection of fresh air enhances deposition of droplets on the surfaces and thus reduces their concentration in the bus. Finally, the analysis identifies an optimal range of temperature, humidity and ventilation rate to maintain human comfort while minimising the transmission of droplets.

1. Introduction

Since late 2019, the transmission of SARS-CoV-2 [1] has significantly affected humankind in the entire world. It has been shown that coughing, sneezing [2], and speaking [3] constitute the main routes of virus transmission. This could be through the deposited droplets over surfaces or the suspended droplets entering the mouth, nose and eyes. Virus-carrying droplets cover a range of sizes, and the larger they are, the more likely they become to deposit on surfaces, while the smaller ones may remain suspended in the air for a long time. It has been argued that these airborne droplets are responsible for virus transmission [2]. It follows that predicting the distribution of such droplets is an essential requirement for understanding the transmission routes of the virus

The suggested 1–2 m social distance by WHO is based on the study of Wells [4] in 1934 assessing the lifetime of droplets. However, the droplets can be carried to further distances if the airflow is considered. Sneezing and coughing are accompanied by complex turbulent respiratory flows, which can be responsible for virus spreading. The interactions between the moving droplets and the airflow break up the droplet and alter the subsequent evaporation and deposition processes. It has been reported that a single sneeze can produce droplets with velocities in access of 10–20 m/s [5]. The larger droplets settle on the surface by the gravitational forces. The smaller droplets, however, are

* Corresponding author at: School of Engineering and Materials Science, Queen Mary University of London, London E1 4NS, United Kingdom.
E-mail address: n.karimi@qmul.ac.uk (N. Karimi).

https://doi.org/10.1016/j.cej.2021.132761
Received 14 July 2021; Received in revised form 21 September 2021; Accepted 29 September 2021
Available online 7 October 2021

Nomenclature

$C_{1M}^{2\sigma}$	Surface vapour mass concentration $[kg.m^{-3}]$
C_{1M}	Mass concentration of gas component $[kg.m^{-3}]$
$C_{M1}^{3\sigma}$	Partial surface concentration of the vapour $[kg.m^{-3}]$
c_3	Constant parameter
D_3	Constant parameter
$D_{M\rightarrow\sum n}$	Hydraulic diameter for the droplet$[m]$
d_p	Diameter of the droplet$[m]$
f_p	Net turbulent force$[N]$
$f_{p,i}$	Net turbulent force in t = i$[N]$
f_{p^*}	Net turbulent force for each phase$[N]$
H^{m^*}	Enthalpy for the kth fluid $\left[kJ.mol^{-1}\right]$
H^m	Enthalpy by the combination of phase-weighted $\left[kJ.mol^{-1}\right]$
$h_{M1}^{3\sigma}$	Specific enthalpy for liquid (phase 1) $\left[kJ.mol^{-1}\right]$
$h_{M3}^{3\sigma}$	Specific enthalpy for vapour (phase 3) $\left[kJ.mol^{-1}\right]$
h_{fg}	Convection heat transfer coefficient for evaporation rate $\left[W.m^{-2}.K^{-1}\right]$
J_w	Evaporation of droplet $[kg.s^{-1}]$
k	Kinetic turbulent energy $[m^2.s^{-2}]$
m^*	kth fluid phase
$n_{m^*}^a$	Normal vector at the interface each phase
p	Total Pressure$[Pa]$
$p_{M1}^{3\sigma}$	Partial surface pressure of the vapour$[Pa]$
P_w	Partial saturated vapour pressure$[Pa]$
P_a	Partial water vapour pressure$[Pa]$
q_H^m	Heat flux for the kth fluid (droplet enthalpy) $[W.m^{-2}]$
q^{m^*}	Heat flux for kth fluid $[W.m^{-2}]$
$S_{m^{m^*}}^{int}$	Interface between phases
$S_{u^{m^*}}^{m^*}, S_{v^{m^*}}^{m^*}, S_{w^{m^*}}^{m^*}$	Source or sink terms
S	Body force$[N]$
S_{ij}	Rate of strain tensor
Sh	Sherwood number
T	Temperature$[K]$
$T_{ambient}$	Ambient temperature$[K]$
$T_3^{1\sigma}$	Temperature of vapour (partial surface)$[K]$
t	Time$[s]$
V_{vent}	air velocity inside the ceiling vent
U^m	Mixture velocity(x direction) $[m.s^{-1}]$
u_{fi}^*	X direction of velocity for each fluid (liquid) zone $[m.s^{-1}]$
u_{fi}	X direction of velocity for fluid (liquid) zone $[m.s^{-1}]$
u_l	Velocity in $\times$ direction for liquid phase $[m.s^{-1}]$
u_j	X direction of velocity based on j row $[m.s^{-1}]$
$u^{m^*}, v^{m^*}, w^{m^*}$	Velocity component for kth fluid $[m.s^{-1}]$
w^m	Mixture velocity (Z direction) $[m.s^{-1}]$
x_j	X direction based on j row
x, y, z	Coordinates

Greek symbol

α^{m^*}	Volume fraction for kth fluid phase
$\mu_T^{m^*}$	Viscosity of the continuous kth phase $[kg.m^1.s^{-1}]$
μ^{m^*}	Viscosity for kth fluid $[kg.m^1.s^{-1}]$
α_3	Constant parameter
ε	Dissipation rate $[m^2.s^{-3}]$
ζ	Relaxation factor (functional)
$\Gamma^{`m^*}$	Favre-averaged quantity
λ^{m^*}	Thermal conductivity for nth fluid phase $[W.m^{-1}.K^{-1}]$
λ^m	Mixture thermal conductivity $[W.m^{-1}.K^{-1}]$
ρ	Density $[kg.m^{-3}]$
ρ^m	Mixture density $[kg.m^{-3}]$
ρ^{m^*}	Density for kth fluid $[kg.m^{-3}]$
ρ_l	Density of the liquid phase $[kg.m^{-3}]$
ρ_{m^*s}	Density for nth fluid in spherical geometry $[kg.m^{-3}]$
Φ_{m^*}	Indicative function of each phase
ρ_{m^*}	Density of each phase (average) $[kg.m^{-3}]$
$\upsilon_{m^*}^a$	Kinematic viscosity each phase $[m^2.s^{-1}]$
$\upsilon_{m^*s}^a$	Surface area of volume each phase $[m^2]$
τ_p	Stress tensor in volume of fluid $[N.m^{-2}]$
τ_{ij}	Stress tensor $[N.m^{-2}]$
$\sigma_{m^*}^s$	Instantaneous area of interface per unit of volume $[m^2]$
ΔT^m	Mixture gradient temperature

Abbreviation

ANN	Artificial neural networks
CFD	Computational fluid dynamic
DER	Droplet evaporation rate $[kg.s^{-1}]$
DNN	Deep neural network
GEKO	Generalised k-Ω
LES	Large eddy simulation
MLP	Multi-Layer Perceptron
MSE	Mean squared error
ML	Machine learning
OEEVM	One equation eddy-viscosity model
PISO	Pressure-implicit with splitting of operators
RH	Relative humidity
RBF	Radial basis function
SIMPLE	Semi-implicit pressure linked equation
SVR	Support Vector Regression
WHO	World health organization
3D-MAGGS	Three-Dimensional Multi-Block Advanced Grid Generation System

transformed into nuclei droplets through evaporation. These airborne droplets can be carried everywhere in an enclosed environment by the natural/forced flow of air. The study of droplet-flow interactions can help understand the complex physics of virus transmission, particularly in enclosed environments such as public transport where the risk of infection is high.

A sneeze is an involuntary reflex of the respiratory system that expels explosive air into the ambient. The transient high-pressure air sprays the mucus into the environment.[6] Experiments showed that the droplets from a single sneeze can be carried by a turbulent gaseous cloud even 7–8 m far from the mouth .[7]This clearly shows the importance of analysing sneezing process in enclosed environments. Numerical analyses have been already successfully employed to simulate the travelling paths of virus-containing droplets; see for example [9]. Such investigations help to examine the efficacy of ventilation systems, design social distance layouts in indoor environments, and provide more effective health care protocols. For instance, by determining a wide range of initial injection velocity, size distribution (40–980 μm), it was suggested that the maximum contamination distance can vary between 1 and 4 m [9,10]. Moreover, using the Monte-Carlo technique, it was shown that smaller droplets could stay suspended in air for a long time, and that the initial velocity has a minor effect on the maximum

suspension time. It was further demonstrated that a droplet with a 2.5 μm size remains suspended for approximately 41 min, whereas a droplet with a 100 μm size falls down after 1.5 s .[8]Also, increasing the relative humidity prolongs the evaporation time of the droplets.[9]

Most recently, a comprehensive simulation of a single sneezing passenger inside a bus was conducted by Mesgarpour and co-workers [10]. The droplets size distribution was calculated by applying the volume of fluid method to the mouth and lips of the infected person. It was shown that the droplets with sizes<250 μm could travel the whole length of the bus. Further, evaporation of the droplets are of significance as it directly affects survival of the droplets and thus their virus carrying potentials [11]. It has been shown that it takes between 2 and 137 s for a droplet with a volume of 1 to 10 mL to completely evaporate over a surface [12]. In recent months, significant attempts have been made to numerically simulate the spread of droplets in public indoor environments, see, for example, Lu et al. [2] , Ren et al. [13] and Khosronejad et al. [14]. These studies indicated that ventilation systems could accelerate the dispersion of droplets in the room, yet they fail to remove the larger droplets before deposition. Abuhegazy et al. [15] showed that the size and location of the airborne droplets are strongly influenced by the ventilation system. The effects of relative humidity and wind velocity on the evaporation and dispersion of the droplets in an open space were evaluated by Li et al. [16]. By numerical simulation of sneezing in a room, Singh and Tripathi developed a model for droplets transmission [17]. Experiments of Chaudhuri et al. [18] showed that the droplets evaporation time depends on the ambient temperature.

Although detailed simulation of the generation and dispersion of virus-carrying droplets is possible, the large number of parameters involved in this problem complicates such simulations. Further, in practice, many large environments with highly complex and varying configurations should be simulated. Hence, the computational time and cost of a purely computational approach would be forbiddingly high. To reduce the computational burden, techniques from Machine learning (ML) can be combined with Computational fluid dynamics (CFD). Such a hybrid approach has been already applied to the problems in aero-propulsion [19], heat and mass transfer [20,21] and spread of coronavirus [10]. In all these, substantial reduction in the computational expenses (up to 99%) was achieved, while predictions remained quite accurate. Given the size, variations and complexities of the indoor environments in which virus is spread, machine learning could significantly facilitate the analysis.

Artificial Neural Networks (ANN) offers an accurate means of prediction on the basis of computational data. The capabilities of this method are already well-demonstrated. For instance, comparing CFD simulations of natural convection in a triangular cavity and ANN indicated that both soft codes predict the stream function and temperature parameters correctly [22]. Similarly, CFD simulation of natural convection of cold column cylinders was compared with a Multi-Layer Perceptron (MLP) network [23]. The training algorithm was resilient back-propagation, and the results indicated a good agreement between the two techniques. Further, ANN can be applied to more complex physics, such as multiphase flows [24] and porous media [26,27]. For example, it was demonstrated that the Levenberg-Marquardt Algorithm (LMA) could replicate the unsteady simulation of a chaotic movement of gas-liquid flow in a square cavity with<10 % error [2]. Further examples of combining CFD and ANN can be found in Refs. [20,21,25–28].

Table 1
Sneezing specifications.

Parameter	Value	Unit	Ref.
Number of droplets (t = 0)	5,000,000	–	[33,34]
Maximum velocity (sneezing)	112	$m.s^{-1}$	
Initial temperature (sneezing)	305	K	
Separation angle (sneezing)	42	Degree	

This study aims to provide a prediction of the distribution of the fine droplets and aerosols (1 ~ 250μm) generated during sneezing. A recent work of the authors showed that these droplets are most responsible for the transmission of the virus as they could travel a long distance before deposition/evaporation [10]. The indoor environment of a bus as an example of a realistic high-risk environment with complex geometry is considered. The influences of ambient temperature and humidity, as well as the effects of ventilation, are investigated using a novel hybridised CFD/ML tool.

2. Problem configuration and flow solvers

The inner space of a bus (Mercedes Benz, Tourismo (SKS E128I) with standard seats (Fig. 1a) is considered. Ambient air is injected from the fresh air duct and is collected by the ducts placed on the ceiling (× 36). Three different air temperatures and relative humidity (RH) are considered for simulations. The ventilation system circulates the air in the bus without affecting the air temperature, and RH. Air leakages are neglected, and the bus is assumed to move with a constant velocity. The range of flow rate for this type of bus is between 800 and 6,600 $m^3.hr^{-1}$, based on the DENSO LD9 HVAC unit [29–32].

Further, the entire bus is assumed to be under thermal equilibrium, and the heat generated by the sneezing person is ignored. Also, only one

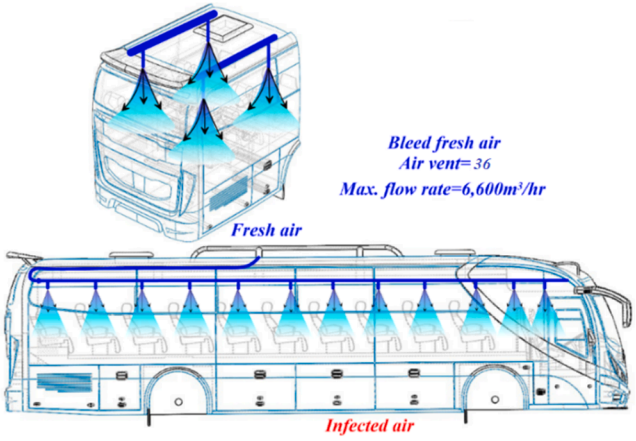

(a)

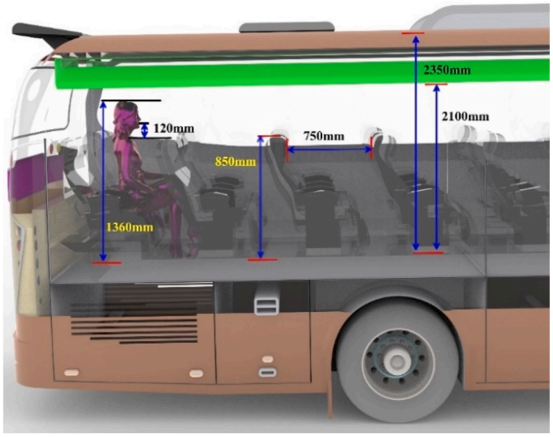

(b)

Fig. 1. Ventilation system and the bus geometry a) HVAC duct based on Refs.[32,34], b) location of the sneezing person.

Table 2
Computational models used in the numerical study.

Model		Type	Index	Range	Ref.
Viscous models	Turbulence zone	LES-RANS	Dissipation rate- Re	$15,000 < Re < 87,320$	[34]
	Transient zone	GEKO	Re- turbulence intensity	$5,300 < Re < 15,000$	[35]
	Laminar model	Laminar Zone	–	$Re < 5,300$	[36]
Evaporation method		Arbitrary-Lagrangian–Eulerian	Droplet diameter	$\text{Upperranged}_{\text{droplet}} < 250\mu\text{mLowerranged}_{\text{droplet}} > 1\mu\text{m}$	[37,38]
Droplet temperature		Non-uniform profile	Temperature gradient of droplet and ambient	Upper range $T_{\text{droplet}} < 37\ ^{\circ}\text{C}$	[39]
Breakup		Simple coupled level set and volume of fluid (S-CLSVOF)	Balance of internal and external force	–	[40]

sneezing passenger inside the bus is considered. Fig. 1b shows the location of the sneezing person in the bus. This passenger is located in the last row of sits and on the left side of the bus, sneezing horizontally and directly forward. This position allows direct transmission of the droplets to the entire internal volume of the bus. The sneezing characteristics are summarised in Table 1.

Throughout the conducted simulations the environmental parameters varied as: air temperature (288.15 K, 305.15 K, and 330 K), ventilation velocity (0.1 m/s, 0.3 m/s, and 0.5 m/s), and relative humidity (20%, 40%, and 60%).

Table 2 summarises the computational models and zones used in the current study. By dividing the calculation domains into three distinctive zones based on dissipation rate and Re, physical phenomena are simulated more accurately.

An in-house code (in Python) was developed to solve the governing equations with second-order accuracy. One hundred and twelve cores were used with a graphic card for simulations. The PISO method of velocity and pressure coupling was employed for turbulent modelling, and the SIMPLE method was used for laminar flow. The obtained solution was time-dependent with a 0.001 s time step over 600 s. ANSYS 2021R1 was used for data post-processing, and the mesh was generated in ANSYS ICEM and implemented directly to the code. In order to enhance the accuracy, the investigated domain was divided into three regions. The zone right in front of the sneezing person was modelled using LES; the transient GEKO model was used for the transition region, and laminar flow was considered for the air movement in the rest of the bus. These three computational zones are demonstrated in Fig. 2.

According to Fig. 2, LES has been used for up to 500 mm from the sneezing person. This is because the high momentum sneezing flow can set a strong turbulent flow around the sneezing person. Between 500 ~ 1500 mm, a turbulence model with low intensity of turbulence was used to model the droplets. It should be noted that evaporation of droplets mostly occurs in this zone. There exists a relaxing zone stretched from 1500 ~ 12000 mm of the sneezing person [10,12]. According to Fig. 2, a numerical simulation is performed in the area marked in red while machine learning is trained at each time step. Validation of machine learning with a numerical solution is done in the green area, while predictions are made by machine learning throughout the entire range marked with blue. The following assumptions are made throughout the proceeding analyses.

1) The seats are considered as solid and smooth surfaces.
2) The walls, ceiling, and windows are assumed to be adiabatic.
3) The head and body movements of the sneezing person during sneezing have been ignored.
4) Sneezing occurs once at the beginning of the analysis, and then the interactions of the ventilation system and droplet distribution are evaluated.
5) The droplets are assumed to be initially spherical particles.
6) In the calculation of droplet shapes, the effects of collisions with surfaces are negligible.

It is noted that most of the findings of the current study remain valid for other forms of public transport (e.g. train) and stationary environments such as classrooms.

3. Mathematical modelling

3.1. Multiphase flow equations

The investigated multiphase flow contains droplets in the range of 1 ~ 250μm (liquid phase), air (gas phase), and vapour phase. The mathematical model includes the conservation equations in the Eulerian framework for any m^* fluid, expressed by [41,42]:

Conservation of mass:

$$\frac{\partial(\alpha^{m^*}\rho^{m^*})}{\partial t}+\frac{\partial(\alpha^{m^*}\rho^{m^*}u^{m^*})}{\partial x}+\frac{\partial(\alpha^{m^*}\rho^{m^*}v^{m^*})}{\partial y}+\frac{\partial(\alpha^{m^*}\rho^{m^*}w^{m^*})}{\partial z}=S^{int}_{m^{m^*}} \tag{1}$$

Balance of momentum in $\times$, y and z directions [43,44]

$$\frac{\partial(\alpha^{m^*}\rho^{m^*}u^{m^*})}{\partial t}+\frac{\partial(\alpha^{m^*}\rho^{m^*}u^{m^*}u^{m^*})}{\partial x}+\frac{\partial(\alpha^{m^*}\rho^{m^*}v^{m^*}u^{m^*})}{\partial y}+\frac{\partial(\alpha^{m^*}\rho^{m^*}w^{m^*}u^{m^*})}{\partial z}=\frac{\partial}{\partial x}\left[\alpha^{m^*}\left(\mu^{m^*}+\mu_T^{m^*}\right)\frac{\partial u^{m^*}}{\partial x}\right]+\frac{\partial}{\partial y}\left[\alpha^{m^*}\left(\mu^{m^*}+\mu_T^{m^*}\right)\frac{\partial u^{m^*}}{\partial y}\right]+\frac{\partial}{\partial z}\left[\alpha^{m^*}\left(\mu^{m^*}+\mu_T^{m^*}\right)\frac{\partial u^{m^*}}{\partial z}\right]+S^{m^*}_{u^{m^*}} \tag{2}$$

$$\frac{\partial(\alpha^{m^*}\rho^{m^*}v^{m^*})}{\partial t}+\frac{\partial(\alpha^{m^*}\rho^{m^*}u^{m^*}v^{m^*})}{\partial x}+\frac{\partial(\alpha^{m^*}\rho^{m^*}v^{m^*}v^{m^*})}{\partial y}+\frac{\partial(\alpha^{m^*}\rho^{m^*}w^{m^*}v^{m^*})}{\partial z}=\frac{\partial}{\partial x}\left[\alpha^{m^*}\left(\mu^{m^*}+\mu_T^{m^*}\right)\frac{\partial v^{m^*}}{\partial x}\right]+\frac{\partial}{\partial y}\left[\alpha^{m^*}\left(\mu^{m^*}+\mu_T^{m^*}\right)\frac{\partial v^{m^*}}{\partial y}\right]+\frac{\partial}{\partial z}\left[\alpha^{m^*}\left(\mu^{m^*}+\mu_T^{m^*}\right)\frac{\partial v^{m^*}}{\partial z}\right]+S_{v^{m^*}}^{m^*} \quad (3)$$

$$\frac{\partial(\alpha^{m^*}\rho^{m^*}w^{m^*})}{\partial t}+\frac{\partial(\alpha^{m^*}\rho^{m^*}u^{m^*}w^{m^*})}{\partial x}+\frac{\partial(\alpha^{m^*}\rho^{m^*}v^{m^*}w^{m^*})}{\partial y}+\frac{\partial(\alpha^{m^*}\rho^{m^*}w^{m^*}w^{m^*})}{\partial z}=\frac{\partial}{\partial x}\left[\alpha^{m^*}\left(\mu^{m^*}+\mu_T^{m^*}\right)\frac{\partial w^{m^*}}{\partial x}\right]+\frac{\partial}{\partial y}\left[\alpha^{m^*}\left(\mu^{m^*}+\mu_T^{m^*}\right)\frac{\partial w^{m^*}}{\partial y}\right]+\frac{\partial}{\partial z}\left[\alpha^{m^*}\left(\mu^{m^*}+\mu_T^{m^*}\right)\frac{\partial w^{m^*}}{\partial z}\right]+S_{w^{m^*}}^{m^*} \quad (4)$$

The balance of energy for the mixture model of multiphase flow is written as [43,45,46]:

$$\frac{\partial(\rho^m H^m)}{\partial t}+\nabla.(\rho^m U^m w^m)=\nabla.(\lambda^m \Delta T^m)-\nabla.\overset{\hat{A}}{q_H^m}+\zeta-\nabla.\sum_{m^*=1}^{2}\left(\alpha^{m^*}\rho^{m^*}U^{dr,m^*}H^{m^*}\right) \quad (5)$$

$$\rho^m=\sum_{m^*=1}^{2}(\alpha^{m^*}\rho^{m^*}) \quad (6)$$

$$\lambda^m=\sum_{m^*=1}^{2}(\alpha^{m^*}\lambda^{m^*}) \quad (7)$$

3.1.1. Viscous model

LES was employed to simulate the vortical flow set by sneezing. The continuity and momentum equations in this method are expressed as [47]

$$\left(\frac{\partial\rho}{\partial t}\right)+\left(\frac{\partial(\overline{\rho u_i})}{\partial x_j}\right)=0 \quad (8)$$

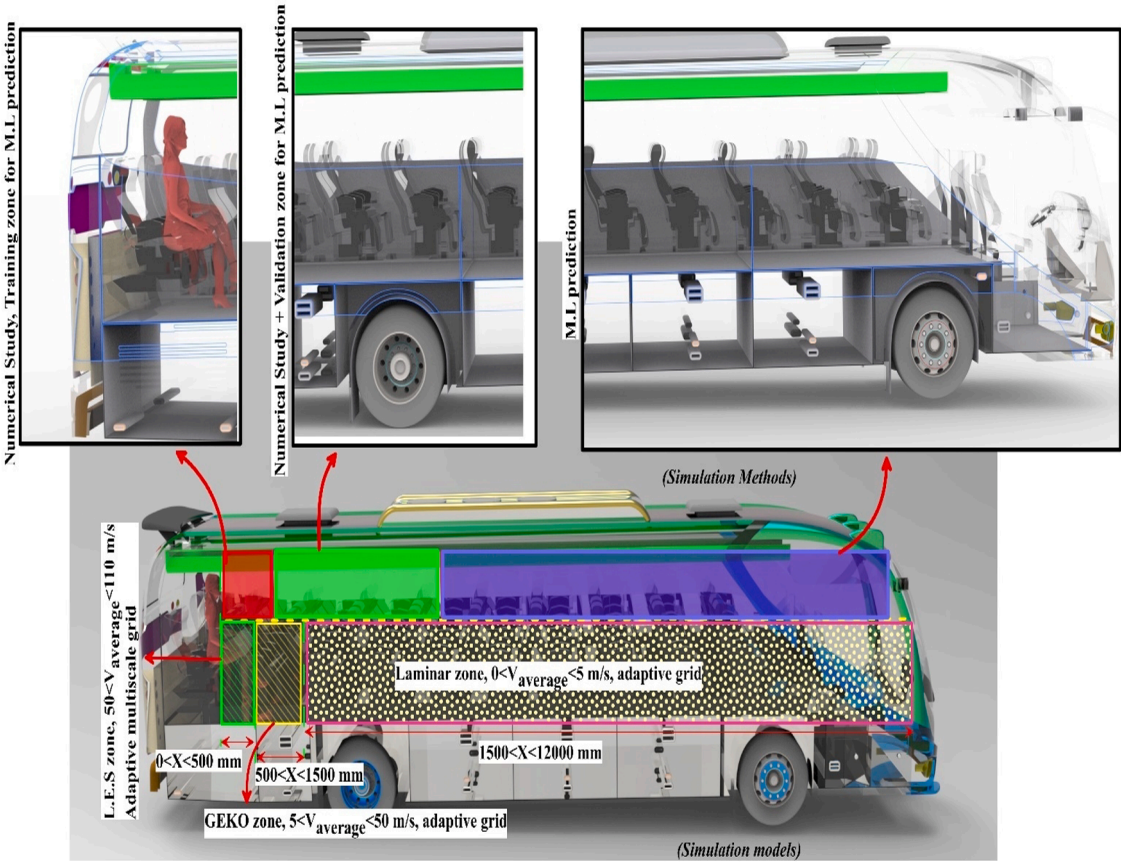

Fig. 2. Demonstration of the three computational zones and the areas for which CFD and ML analyses were conducted.

$$\left(\frac{\partial(\overline{\rho u_j})}{\partial t}\right)+\left(\frac{\partial(\overline{\rho u_i u_j})}{\partial x_j}\right)=-\left(\frac{\partial p}{\partial x_j}\right)+\left(\frac{\partial \sigma_{ij}}{\partial x_j}\right)-\left(\frac{\partial \tau_{ij}}{\partial x_j}\right)+S \tag{9}$$

In this equation, the term S defines the body forces applied to the fluid. The stress tensor τ_{ij} is expressed by

$$\tau_{ij}=\rho\left(\overline{u_i u_j}-\overline{u_i}\,\overline{u_j}\right) \tag{10}$$

$$S_{ij}=\frac{1}{2}\left(\frac{\partial(\overline{u_j})}{\partial x_i}+\frac{\partial(\overline{u_i})}{\partial x_j}\right) \tag{11}$$

where S_{ij} is the rate of the strain tensor. To calculate the turbulence kinetic energy (k), the following one equation eddy-viscosity model (OEEVM) was employed.

$$\partial(\overline{\rho}k)+\nabla.(\overline{\rho}ku)=-\tau_{ij}.S_{ij}+\nabla.(\mu_k\nabla k)+\overline{\rho}\varepsilon \tag{12}$$

$$\varepsilon=c_3 k^{3/2}/\Delta \tag{13}$$

The kinetic energy in the LES sub-grid model is defined by [48]:

$$\langle u_i\frac{\partial f_{p,i}}{\partial f_p}\rangle^*=u_i\frac{\partial\langle f_p\rangle^*}{\partial f_p} \tag{14}$$

$$\frac{\partial\langle f_p\rangle^*}{\partial t}+u_i\frac{\partial\langle f_p\rangle^*}{\partial x_i}+\frac{\partial}{\partial u_i}\left[\frac{1}{\tau_p}\left(\langle U_{fi}\rangle^*-u_i\right)\langle f_p\rangle^*\right]=-\frac{1}{\tau_p}\frac{\partial\langle u_{fi}^* f_p\rangle^*}{\partial u_i} \tag{15}$$

where $u_f^*=(U_f|C)-\langle U_f\rangle^*$. Considering Boussinesq approximation, a simple correlation for the incompressible Reynolds stress tensor is given by:

$$\overline{\overline{u_i^o u_j^o}}=2/3k\delta_{ij}-v_T\left(\frac{\overline{\overline{u_i^o}}}{\frac{\partial x_j+\overline{\overline{u_j^o}}}{\partial x_i}}\right) \tag{16}$$

The transfer of data between LES and RANS is based on the procedures in Refs [49–51] and are not further discussed here.

3.2. Physical characteristics of sneezing

3.2.1. Sneezing profile

The saliva droplets leave the mouth with a time-dependent sneezing profile. The considered exit velocity profile and pressure variation of sneezing are based on that in Ref. [6], and therefore the maximum exit velocity was set to 100 ($m.s^{-1}$). Further, there is a no-slip boundary condition for the flow inside the mouth. In keeping with the literature [52,53], the exit sneezing flow is set to have a relative humidity of 75%, while the droplets' temperature is between 34 ℃ and 36℃. Also, the droplets are assumed to have a uniform distribution with a perfectly spherical shape at the exit moment [5,6]. The physical properties of the saliva are based on those in Refs. [6,54,55].

3.2.2. Droplets

In each time step, the droplet diameter was calculated following the methodology introduced in Refs. [12,43]. Further, the merging of the droplets was modelled on the basis of the analysis detailed in Refs. [56,57]. The droplets generated by sneezing have a size in the range of 1 and 1000 μm while, only those with diameters between 1 and 250 μm could travel a long distance [10,34]. The droplets' shape changes significantly during the advection process affecting their distribution, stability and suspension time. The droplet shape is calculated by considering the external and internal forces in each time step. These include drag force, droplets breakup, and collisions. Fig. 3 shows the variations of droplet mass and drag force with time and Reynold number, respectively. Expectedly, the droplet mass decreases over time [58] while drag force is calculated [38,59,60]. In Fig. 3a, the outcomes of adaptive method (boundary layer adaptation with geometry) have been compared with those provided by two other methods (bulk zone method [61,62], regular method [63]) extracted from literature. Clearly, the adaptive method offers predictions closely matching the benchmark data. Similarly, Fig. 3b shows that the adaptive methods can successfully predict the drag force in comparison to spherical shape [64] and deformable spherical shape [65,66].

3.2.3. Heat and mass transfer in sneezing process

3.2.3.1. Droplet temperature profile. Temperature distribution inside the droplet is central to the modelling of droplet evaporation. Temperature distribution models are categorised based on the surface temperature distribution and ambient temperature. The current study utilises four

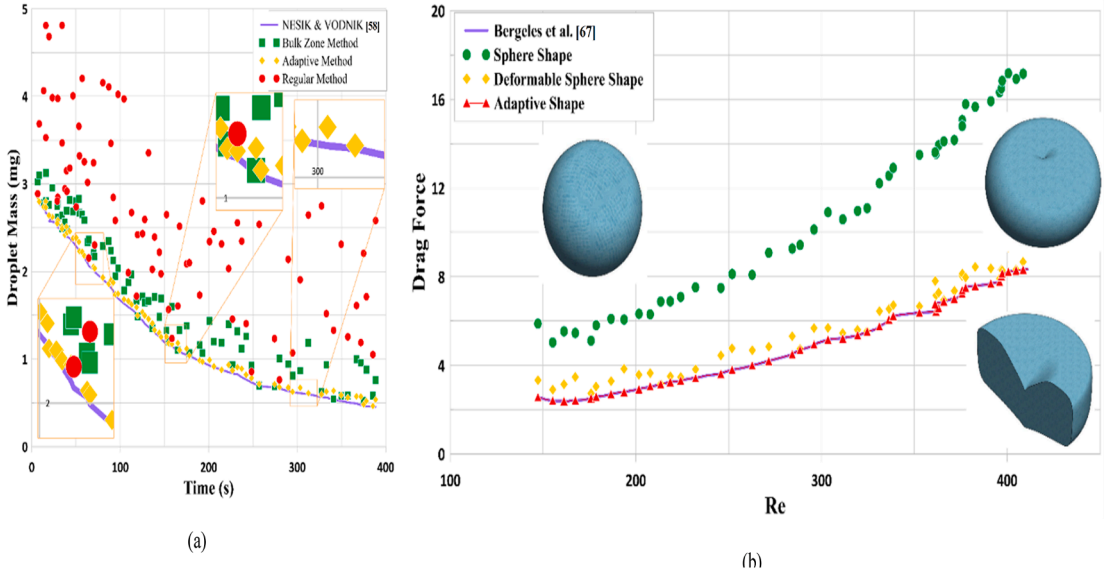

(a) (b)

Fig. 3. Prediction of a) droplet mass variation with time calculated by three different models and b) drag force based on Refs. [58,67].

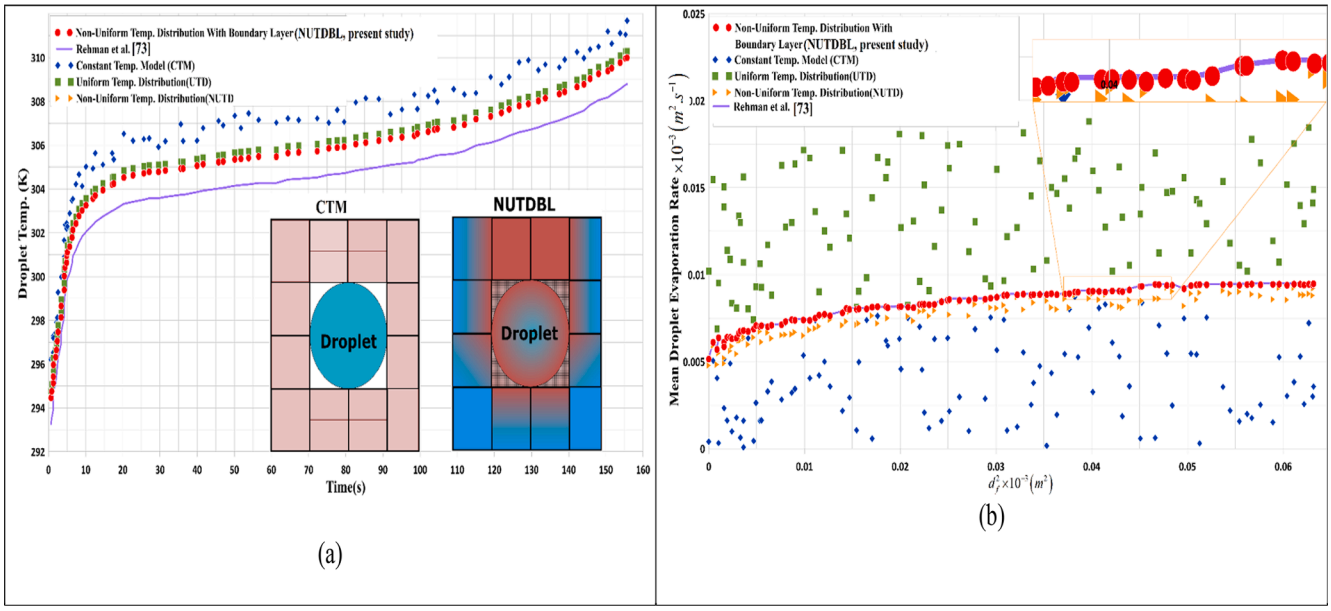

Fig. 4. Comparison between different temperature distributions, a) temporal variation of the droplet internal temperature [73] and b) mean droplet evaporation rate base on droplet surface [73].

different models, including constant temperature model [68], uniform temperature model [69], non-uniform temperature distribution [70] and non-uniform temperature distribution with boundary layer [71,72], to calculate the droplet evaporation rate and its temperature distribution. The results have been compared with those reported in Ref. [73] (see Fig. 4a). Evidently, the non-uniform temperature distribution with boundary layer model [72] and adaptive computational domain on the non-spherical shape of the droplet could provide the most accurate estimation of the droplet temperature. The droplet mass variation with evaporation alters the droplet mean diameter, which then changes the droplet deposition rate. Here, the calculation of droplet internal temperature is on the basis of the boundary layer sensitivity to accurately calculate the droplet temperature distribution. Indeed, the computational domain next to the outer droplet shell adapts itself to the droplet shape with an assumed isothermal boundary. Fig. 4b shows a variation of the mean droplet evaporation rate with the mean surface area. The results shown in Fig. 4 confirm that the new model offers an accurate prediction of the droplets evaporation rate.

3.2.3.2. Mass transfer and evaporation process. The mass transfer for any m^* fluid is governed by the following equation [43,45].

$$\frac{\partial}{\partial t}\left(\rho_{m^*}\Phi_{m^*}\right)+\frac{\partial}{\partial x_\alpha}\left(\rho_{m^*}\Phi_{m^*}v^\alpha_{m^*}\right)=-\rho_{m^*s}\left(v^\alpha_{m^*s}-v^\alpha_s\right)n^\alpha_{m^*}\sigma^s_{m^*} \tag{17}$$

For vaporisation processes, if the droplets kinetic energy and the viscous dissipation are ignored, the mass transfer on the droplets interface can be approximated by [74]:

$$\Gamma^{om^*}=\frac{\sum m^*\left\langle\overline{q^{m^*}\nabla_x}\right\rangle}{hfg} \tag{18}$$

Combining the enthalpy and mixture velocity for integration of the phase and mass-weighted variables yields [45]:

$$U^m=\frac{\sum_{m^*=1}^{2}\left(\alpha^{m^*}\rho^{m^*}U^{dr.m^*}\right)}{\sum_{m^*=1}^{2}\left(\alpha^{m^*}\rho^{m^*}\right)}$$

$$H^m=\frac{\sum_{m^*=1}^{2}\left(\alpha^{m^*}\rho^{m^*}H^{m^*}\right)}{\sum_{m^*=1}^{2}\left(\alpha^{m^*}\rho^{m^*}\right)} \tag{19}$$

In equation 48, U^{dr,m^*} is the drift velocity for the m^*th phase, which can be defined as $U^{dr,m^*}=U^{m^*}-U^m$. The evaporation of droplets is modelled using [75–77]:

$$J_w=1\times10^{-6}\left(20.56+27.21V_a+6.392V_a^2\right)\left(1\times10^{-3}\left(P_w-P_a\right)\right)^b$$

$$b=1.22-0.19V_a+0.0387V_a^2 \tag{20}$$

According to Eq. (20) the decreasing flux of evaporating mass can be estimated by balancing energy and mass on both sides of the interface [43]. *Stefan*'s correlation was used to find the concentration of vapour on the interface of the droplet; the mass concentration for each phase is given by [15,62,75,77,78]

$$C^{2\sigma}_{1M}=1-(1-C_{1M})exp\left(\frac{D_3^2}{6\alpha_3\rho_1 shD_{M\to\sum_n}}\frac{\chi_3^{1\sigma}\left(T_3^{1\sigma}-T_3\right)}{h^{3\sigma}_{M1}-h^{3\sigma}_{M3}}\right) \tag{21}$$

The concentration equation is now substituted into the body force equations. This yields

$$p^{3\sigma}_{M1}=p\frac{c^{3\sigma}_{M1}}{M_{M1}}\Big/\left[\frac{c^{3\sigma}_{M1}}{M_{M1}}+\frac{1-c^{3\sigma}_{M1}}{M_{1n}}\right] \tag{22}$$

The droplet evaporation rate is then calculated by the following equation (see Ref. [73] for further details).

$$DER=\frac{d_o^2-d^2}{t_{evaporationrate}} \tag{23}$$

3.3. Machine learning

In this study, four standard and robust artificial neural networks have been used for prediction. In several experiments, these networks' accuracy has been compared in our problem, and the best network has been selected. In the following, the examined networks are briefly introduced. Of course, since the Multi-Layer Perceptron (MLP.) network has provided the best results, this network will be presented in more detail. An MLP network consists of simple operational elements, most of which can work in parallel. These elements, called neurons, are inspired by biological nervous systems. An artificial neuron comprises inputs, outputs, weights, biases, and an activation function. The neural network configuration is determined by the characteristics of each neuron and how they are connected. MLP. has been used to estimate complex

functions in a variety of contexts and articles[79]. The network generally consists of the input layer, the hidden layer, and the output layer. If needed, several hidden layers can be used. Data is injected into the network through the input layer. If $n(ML)$ is the number of input features of the model, this layer contains $n(ML)+1$ neurons. One of the neurons is used as a bias, and the other neurons are used to receive inputs. The hidden layer consists of $m(ML)+1$ neurons, one of which acts as a bias, and the other neurons, using eq. (23), apply an activation function ($g(ML)$) to the weighted sum of the outputs of input layer.

$$f_j = g\left(w1_{0,j} + \sum_{i=1}^{n} w1_{i,j}x_i\right) \tag{24}$$

$$f_j(M.L) = g(M.L)\left(w1_{0,j}(M.L) + \sum_{i(M.L)=1}^{n(M.L)} w1_{i,j}(M.L)x_i(M.L)\right) \tag{25}$$

In this equation, $x_i(M.L)$ and $f_j(M.L)$ are the values of the i-th neuron of the input layer and the j-th neuron of the hidden layer, respectively. $w1_{0,j}(M.L)$ and $w1_{i,j}$are the weights of the bias and i-th input neuron connection with the j-th hidden neuron, respectively. The function $g(ML)$ has different types, some of which are: Sigmoid, Softmax, Hyperbolic, and Rectifier. The output layer is the last layer of the MLP. network. The number of neurons in this layer is equal to the number of model outputs. The neurons in this layer, similar to the hidden layer neurons, use an activation function on the weighted sum of the previous layer outputs with eq. (23) to generate the model output.

$$y_z = g\left(w2_{0,z} + \sum_{j=1}^{m} w2_{j,z}f_j\right) \tag{26}$$

$$y_z(M.L) = g(M.L)\left(w2_{0,z}(M.L) + \sum_{j(M.L)=1}^{m(M.L)} w2_{j,z}(M.L)f_j(M.L)\right) \tag{27}$$

$y_z(ML)$ is the output of z-th neuron of the output layer. $w2_{0,z}$ and $w2_{j,z}$are the weights of the bias and j-th hidden neuron connection with the z-th output neuron, respectively. The activation function of output layer neurons can be different from that of hidden layer neurons. One of the essential characteristics of a neural network is its ability to learn. We used the supervised learning method to train the network. First, connection weights are randomly assigned. After that, the output of the hidden layer neurons and then the output layer neurons are calculated using eqs. (26) and (27). Afterwards, the weights change according to a specific learning algorithm. Weight changes should be made so that the neuron outputs are close to the actual outputs. The process of changing the neuron weights to achieve the desired output is called learning. A loss function is used to evaluate learning performance. The goal of learning is to reduce the amount of loss function to near zero. Therefore, an optimisation algorithm is used to find the weights that minimise the loss function. In this paper, the error backpropagation method is considered as the optimisation algorithm and the Mean Square Error (MSE) criteria as the loss function. The MSE is calculated by eq. (28).

$$MSE = \frac{1}{n}\sum_{i=1}^{n}(O_i - T_i)^2 \tag{28}$$

$$MSE(ML) = \frac{1}{n(ML)}\sum_{i(ML)=1}^{n(ML)}(O_i(ML) - T_i(ML))^2$$

$n(ML)$ is the number of samples. $O_i(ML)$ and $T_i(ML)$ are the model output and target value for sample $i(ML)$. In this paper's implementation of the MLP network, some configuration parameters are: A hidden layer with 35 neurons, the activation function of the hidden and output layer neurons are a hyperbolic tangent sigmoid transfer function, the epoch value equals 300.

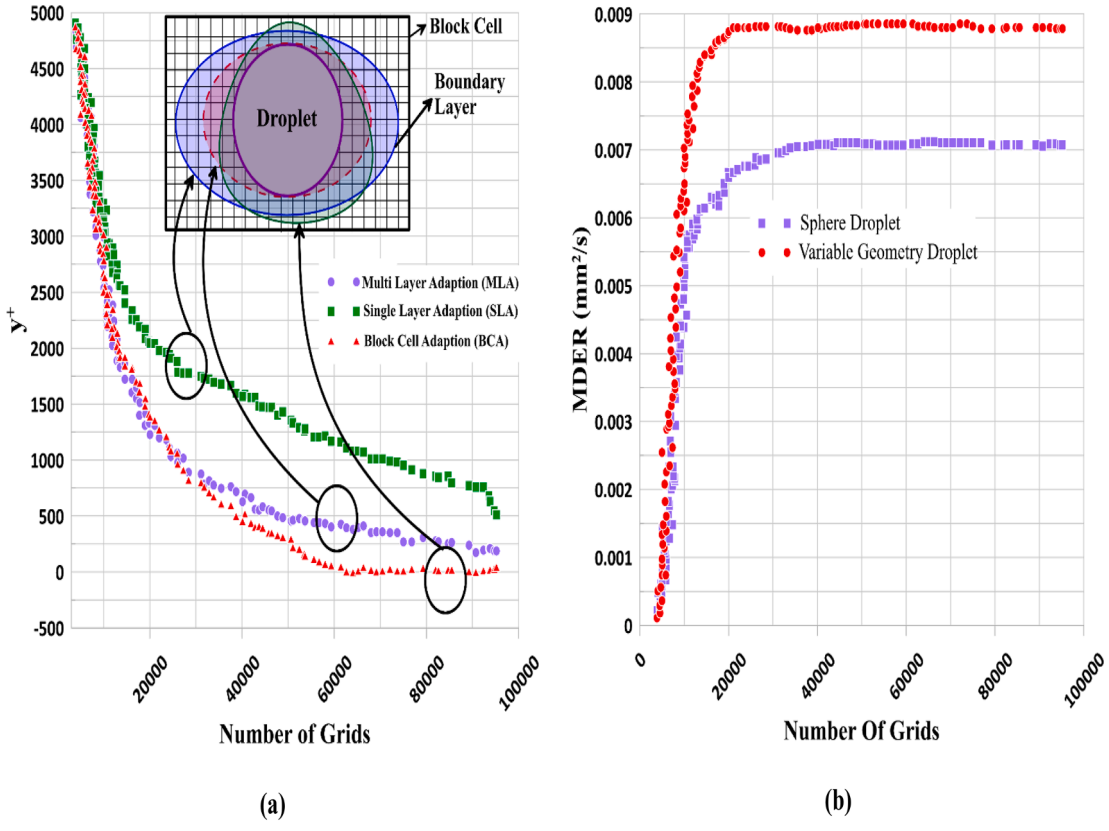

Fig. 5. Multilayer with dual inflation method **a)** y^+ study and **b)** mean droplet evaporation rate based on many grids.

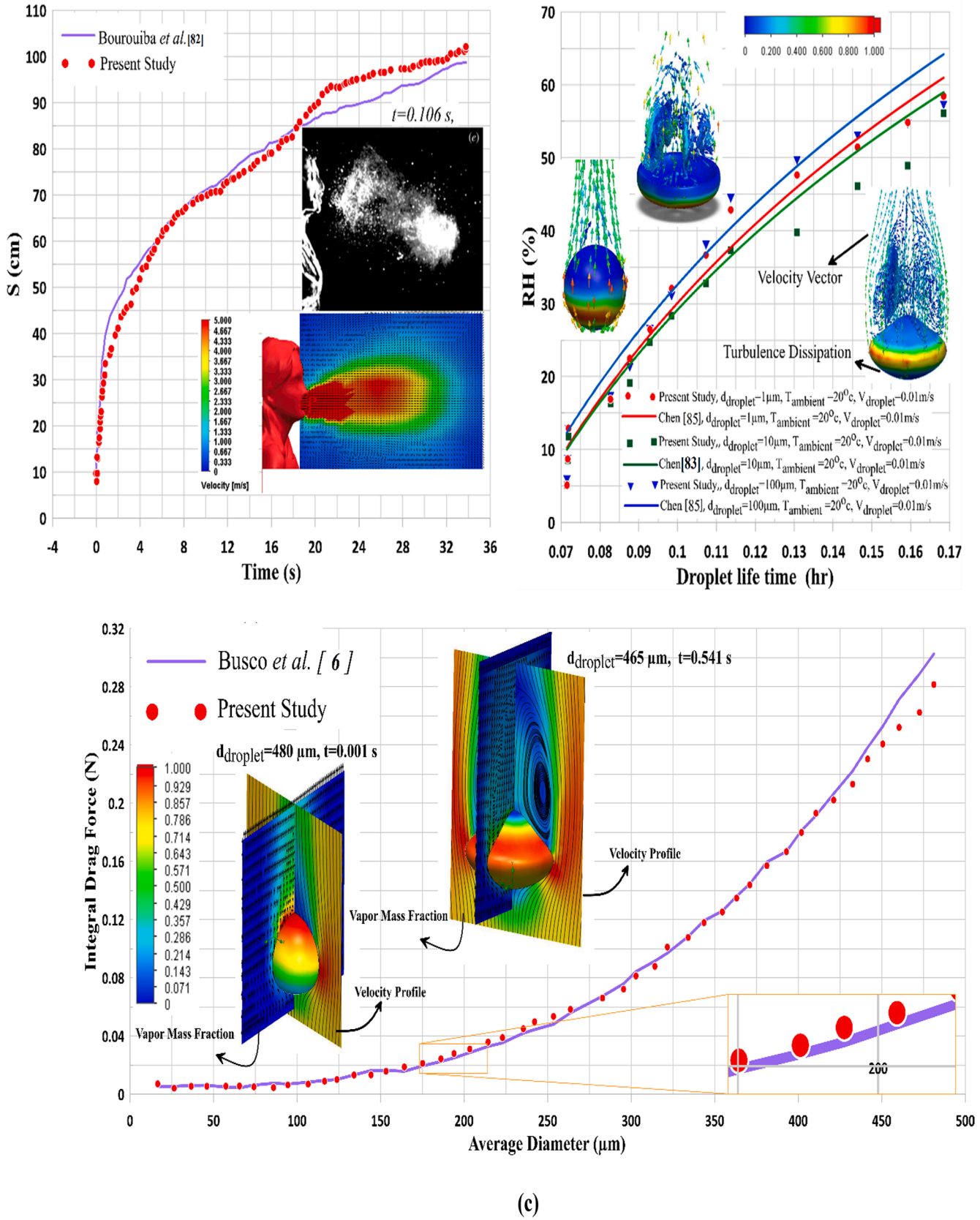

Fig.6. Validation of numerical simulations based on a) diffuse parameter per second [82], b) droplet lifetime based on humidity [83], c) integral drag force based on average diameter [6].

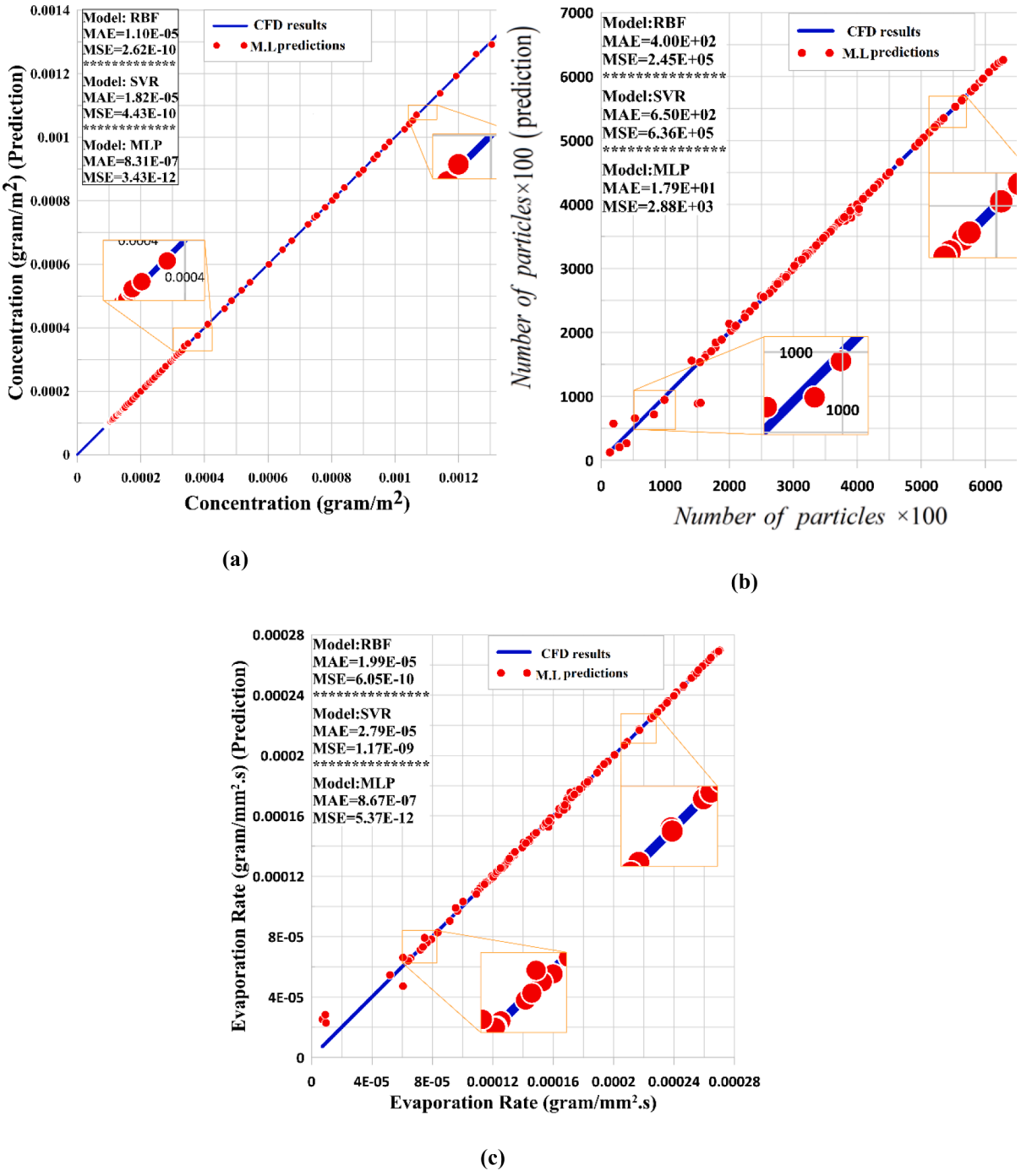

Fig. A1. Comparison between the ML and CFD based on a) droplets concentration, b) number of particles and c) Evaporation rate at X = 10,000 mm, $V_{vent} = 0.1m.s^{-1} T_{vent} = 288.15K$, RH = 20%.

4. Computational grid generation and validation

4.1. Grid generation

The computational grid production in this analysis features significant complexities. The presence of droplets with variable geometry and micron size, the vapour layer and the large dimensions of the bus necessitates taking a novel approach to producing an adaptive grid. Hence, a fully automated algorithm based on the Three-Dimensional Multi-Block Advanced Grid Generation System (3DMAGGS) [80,81] was utilised. In this method, the block separation pattern was applied to separate the areas required for re-meshing. An independent algorithm, based on the vertical velocity profile, created boundary layer grids around the droplets. Fig. 5 shows the grid independency diagrams for different modes. It should be noted that this grid adaptation varied at each time step according to the droplet geometry. Therefore, the grid matching code was based on the droplet geometry to redefine the new grid based on the modified geometry.

4.2. Validation

All developed computational models of sneezing were validated against the existing data extracted from the literature. Fig. 6 provides a comparison between these datasets. Evidently, the current simulation

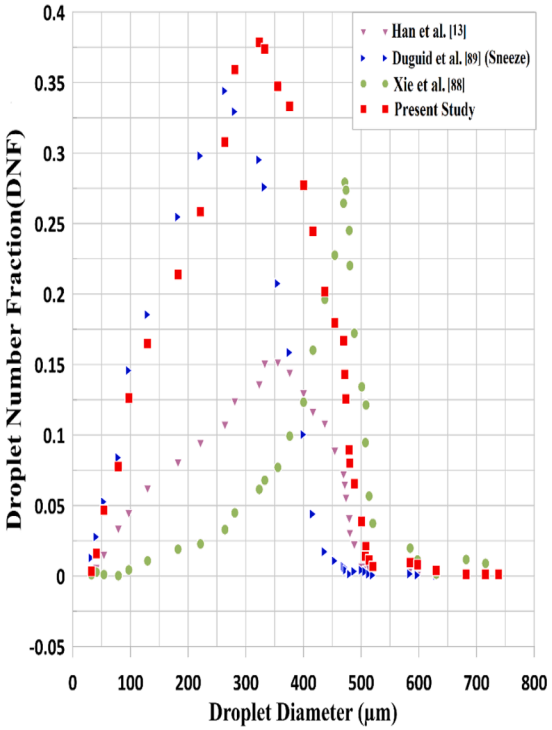

(a)

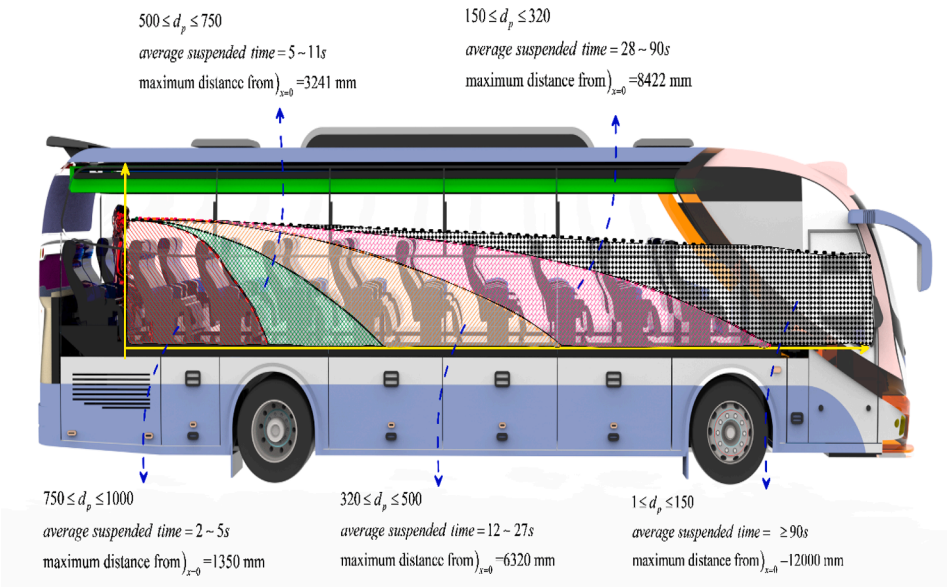

(b)

Fig. 7. a) Droplet number fraction vs time, without ventilation, $T_{ambient}$=298.15 k, RH = 20% [12,86,87]. b) Droplet distribution in the bus ($T_{ambient}$ = 298.15 k, RH = 20%, t = 600 s).

data very well match those extracted from the references.

Given that the machine learning results were extracted from mathematical equations, it is necessary to present the validation of the machine learning results. The validation of machine learning in this case study is based on numerical simulation, which is available in Appendix A - Fig. A1.

5. Results and discussions

5.1. Sneezing process

The propagation spectra of different sneezing droplets are depicted in Fig. 7a, illustrating the significant effects of the environmental parameters. It has been already shown that the majority of the particles produced by sneezing have a short lifetime and cannot travel a long distance [10]. Here, an air-floating droplet is defined as a measure for

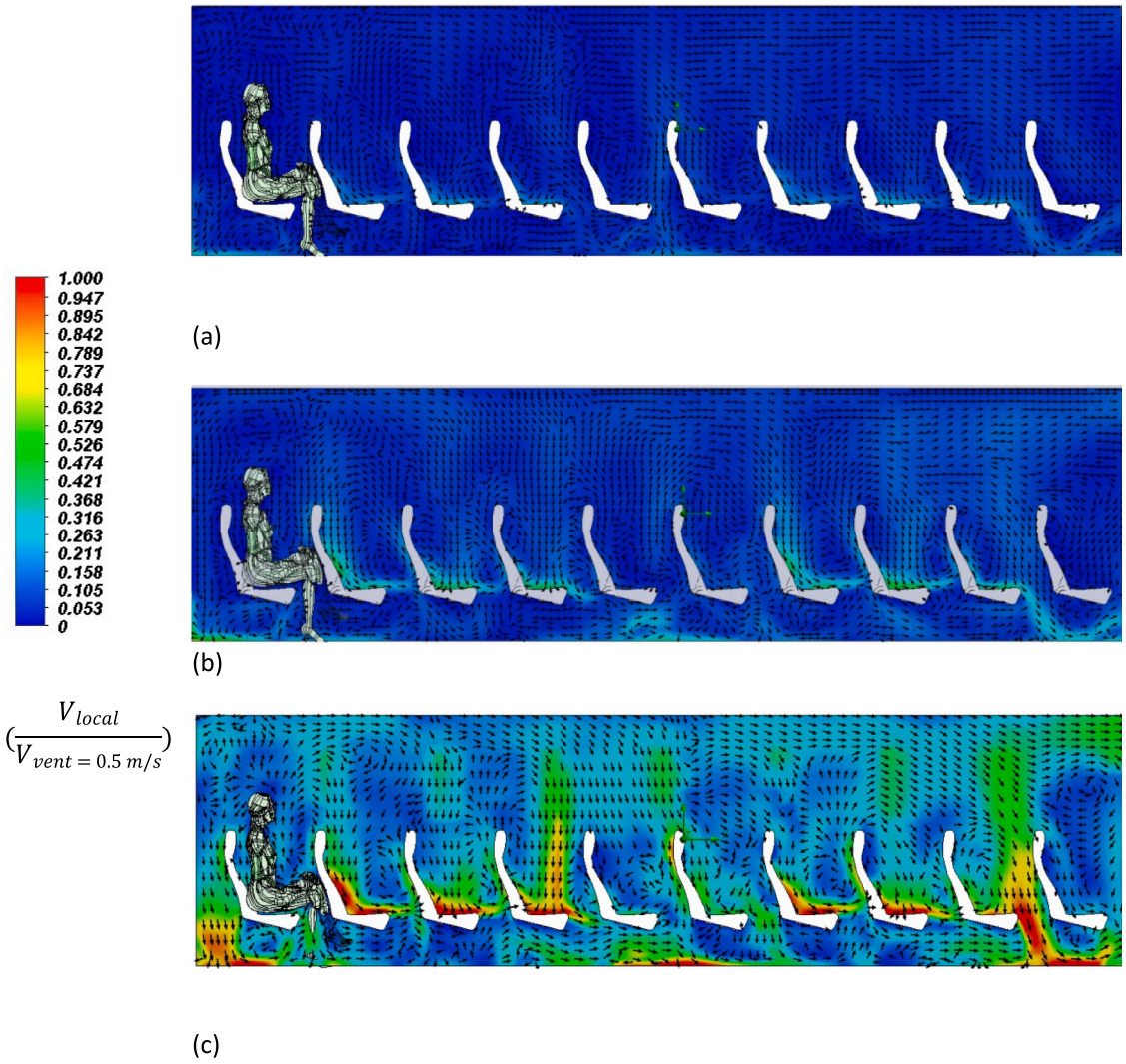

Fig. 8. Non-dimensional flow velocity inside the bus for a)V_{vent} = 0.5 m/s, b)V_{vent} = 0.3 m/s, c)V_{vent} = 0.1 m/s, ($T_{ambient}$ = 330 K, RH = 20%).

95% of particles with similar diameters, which have the following features.

1) Their standard momentum deviation is below 3%.
2) Their velocity is non-zero.
3) The standard deviation of their mass falls below 10%.

Two types of droplets can be found in the range of 1–250 μm: those initially produced at this range and those experiencing evaporation and breakdown along the path. The former rapidly joins other droplets or evaporate due to their high velocity when leaving the mouth, while the latter mainly constituents the transmitted droplets to the other parts of the bus. The important point in this diameter range is the direct relation between the deposited droplets and their dimensions. With the decline in diameter, deposition of the droplets smaller than 25 μm becomes progressively more unlikely. Many references have considered the aerosols with sizes below 5 μm to be largely non-depositing particles [15,84]. Environmental parameters can influence the propagation of droplets generated by sneezing through controlling the evaporation rate and droplet size [18,85]. These effects are investigated in the current section.

In Fig. 7b, the interior space of the bus is divided into a few distinctive zones based on the distribution of sneezing droplets. It is observed that decreasing the diameter of droplets increases the average suspension time and distance. According to Fig. 8a, when the passenger sneezes at the rear end of the bus, the entire interior space of the bus is affected. The provided supplementary data show the average velocity, concentration, and suspension time for all droplet diameters for the duration of 600 s after sneezing. The results indicate that as the droplet diameter decreases, the suspension time increases. Also, droplets become smaller as longer distances are taken from the sneezing passenger [10].

5.2. The effects of the HVAC system

The heating, ventilation and air conditioning system in the bus can significantly influence virus transmission by adjusting the inflow velocity, temperature, and relative humidity. In this investigation, the air is circulated with different velocities, temperatures, and relative humidity inside the bus in accordance with the data provided by the bus manufacturer [30,32].

Fig. 8 shows the steady flow fields set inside the bus by the ventilation system (see Fig. 1). Their different ventilation flow rates have been investigated in this figure. Formation of a complex flow due to the interactions between the seats and ventilation flow is evident. In particular, Fig. 8 shows that intensification of the ventilation rate results in the

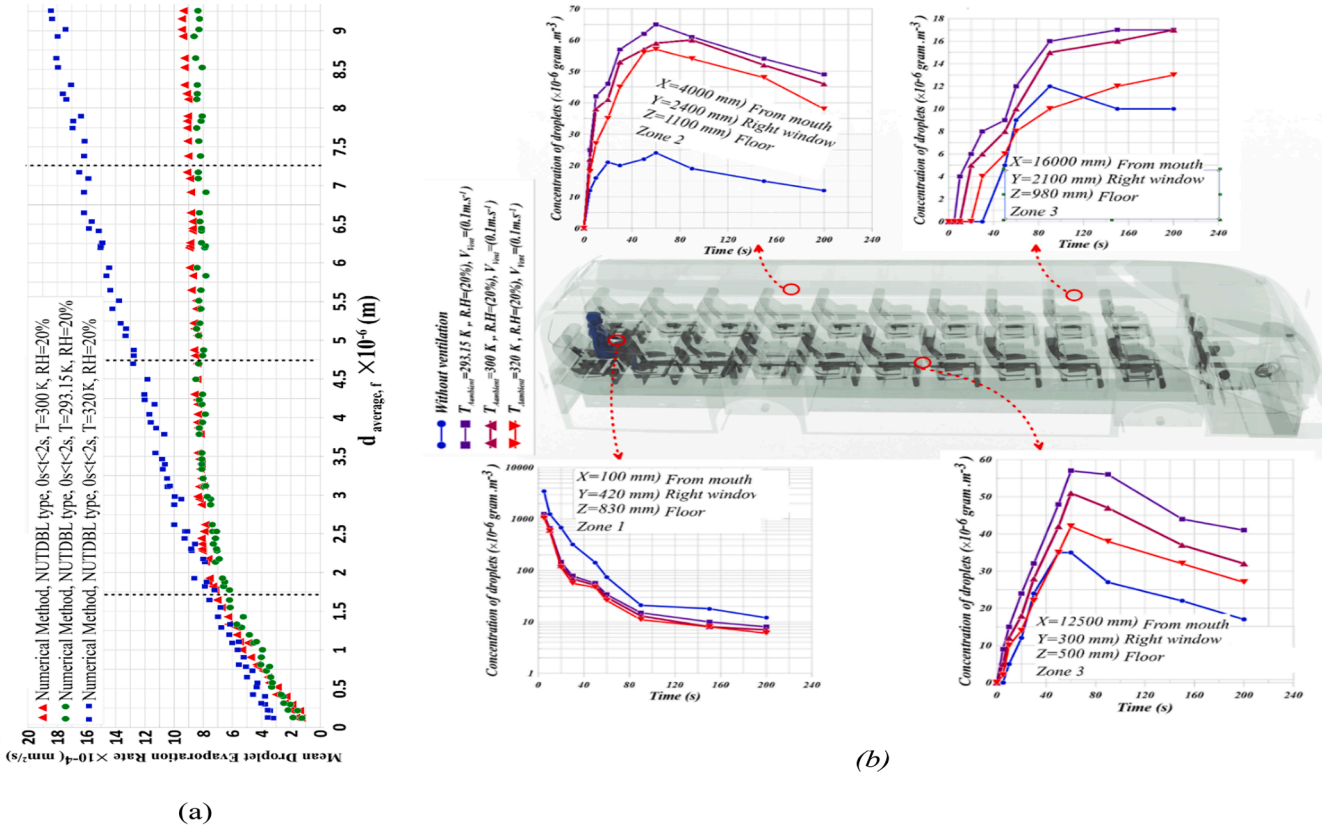

Fig. 9. a) Evaporation rate based on droplet surface for 2 s, $V_{vent} = 0.1(m.s^{-1})$, RH = 20% (numerical simulations and ML predictions), b)Variation in the concentration of droplets ($1\mu m < d_p < 250\mu m$) at various locations over time. Boundary condition for no ventilation is based on Ref. [10].

development of a series of vortical structures between the seats. Importantly, these vortical flows constantly evolve along the bus, and there is, essentially, no repeated pattern. It will be shown that this complex flow significantly influences the virus transmission in the bus.

5.3. Effects of environmental conditions on the droplet suspension time

5.3.1. Temperature variations

Temperature dominates the evaporation rate, and therefore the droplet volume is proportional to the ambient temperature. The air temperature may also have an effect on the droplet viscosity and thus on the shell deformation. Here, assuming constant relative humidity and airflow inside the bus, the effects of temperature on the droplet diameter

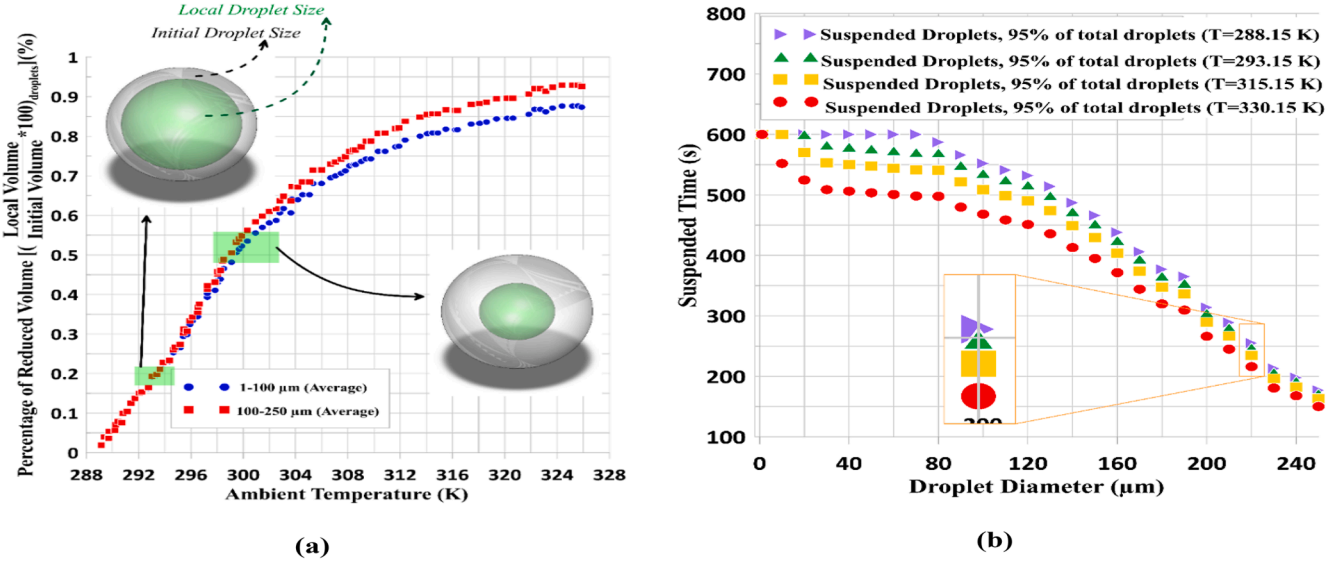

Fig. 10. ML predictions for a) percentage of reduced droplets base on ambient temperature for ($1\mu m < d_p < 100\mu m$) and ($100\mu m < d_p < 250\mu m$) diameter, $V_{vent} = 0.1m.s^{-1}$, RH = 20% b) suspension time based on droplet diameter, $V_{vent} = 0.1m.s^{-1}$RH = 20%.

and floating time is investigated. Here, 5 million droplets, produced at the onset, are analysed using the developed machine learning model (see Section 3.3). This method lowers the computational costs and, more importantly, enables pattern recognition.

The evaporation rate of the propagated droplets is dominated by the surface area exposed to the flow. During the first second after sneezing, the maximum evaporation rate was observed due to the larger dimensions of the droplets and their breaking down. Fig. 9a shows the mean values derived for the droplet shell at the first two seconds subsequent to sneezing. Clearly, there is a substantial geometrical variation in the droplets. Further, increases in temperature significantly enhance the evaporation rate. Fig. 9b illustrates the concentration of droplets ($1\mu m < d_p < 250\mu m$) in various locations throughout the bus. The results show that different locations are exposed to a range of concentrations at different times. Additionally, ventilation noticeably increases the rate of dispersion. As depicted in Fig. 9 b, the highest concentration of droplets is found near the person. There is no noticeable difference between ventilation and non-ventilation conditions in this zone. Additionally, the results indicate that variations in ambient temperature have a negligible effect on the droplet concentration in zone 1. Yet, concentration of droplets in zone 2 increases over time. In zone 2, the number of droplets in the control volume increases as time and ventilation pass. This indicates that ventilation can accelerate the rate of concentration increase in this zone. Additionally, it is clear that reducing the temperature aids in increasing the concentration. After a few seconds, the number of droplets in zone 2 decreases as sneezing creates a progressive front of droplets, and the droplets' concentration decreases along the bus. Most importantly, nowhere in the bus is clear of droplets.

A decline in the droplet diameter results in the enhancement of the floating time. Fig. 10a shows the percentage of the droplets removed from the environment (through evaporation) at the ventilation rate of 0.1 $m.s^{-1}$ and relative humidity of 20% for diameters of 1 ~ 100 μm and 100 ~ 250 μm. As expected, the results indicate that a greater percentage of droplets are eliminated at higher ambient temperatures. Fig. 10b shows the average suspension time for 95% non-spherical droplets in different ranges. The period of suspension is determined by internal and external forces acting on the droplet volume. Since the geometry of the droplet changes over time by the drag force, the suspension time is proportional to the drag force. Additionally, considering the impact of temperature on the droplet viscosity and its effect on the rate of evaporation, it is clear that the geometry of the suspended droplet is determined by the change in the outer shell (due to drag) and the rate of mass reduction. Fig. 10b depicts the considerable effects of temperature upon the suspension time of droplets.

5.3.2. Ventilation rate

Along with directly affecting the distribution of heavy particles in the near field region, ventilation can also have an effect on the droplets' diameter. Further, increasing the airflow velocity speeds up evaporation and increases the frequency of the droplets of less than $100\mu m$ in diameter. The flow velocity inside the bus may also affect the forces acting on the droplets altering the buoyancy and drag forces. This, in turn, influences the particle lifetime and transmission range. Additionally, as shown in Fig. 8, increasing the airflow velocity intensifies the vortex formation between the seat rows in the bus. These vortices can alter the path of the droplets, as droplets, less than $250\mu m$ in diameter tend to follow the flow [88]. Increased airflow rates also help to disperse the heavy droplets, giving them a longer time to evaporate and shrink in size. Table 3 summarises the results for droplet velocity, suspension, and deposition. This table shows that the droplets with diameters less than $20\mu m$ were distributed evenly throughout the bust in 600 s, with over 95% of them remaining floating. As an important observation, it appears that boosting the ventilation velocity can prolong the suspension time.

The transmission of contaminated droplets in the bus is constantly interrupted by the deposition process and re-circulation of air set by the ventilation system. Changes in the ventilation velocity can alter the duration of droplet transmission and suspension. Nonetheless, the details of these modifications are complicated due to the geometrical complexity of the current problem.

It is recalled that the ventilation velocities considered in this study have been inferred from the bus manufacturer's data [32,34]. Fig. 11 shows the average evaporation rate and concentration of droplets, indicating that for $V_{vent} = 0.1m/s$ the evaporation rate of droplets remains almost constant$\left(8\ 9 \times 10^{-4} mm^2.s^{-1}\right)$. The calculations show that for reducing 10% of the mass of a spherical droplet $(1\ 50\mu m)$, the surface velocity of droplet should increase by 19 ~ 21%. For the droplets with $(50\ 120\mu m)$and$(120\ 250\mu m)$, this increase is 15 ~ 17% and 10 ~ 12%, respectively. The change in the droplets' volume as a function of air velocity is depicted in Fig. 11a. According to this figure, increasing the airflow velocity causes an ascending trend in the droplets' evaporation rate, which then stabilises at a constant value. The slope of the diagram changes due to the interactions between the rate of surface evaporation and the heat flux across the droplet surface.

According to Fig. 11b, increasing the ventilation velocity significantly increases the rate of droplet dispersion (up to 41% in zone 2 and 36% in zone 3 compared to without ventilation). The variations in ventilation velocity affect the droplet concentration in zone 1 by up to 50% when $Vvent = 0.5m/s$. However, the concentration of droplets in zone 2 increases over time, and ventilation velocity contributes to reaching the maximum concentration in a short time (59×10^{-4}grams/mm^3 in 44 s). In fact, ventilation velocity has a significant effect on increasing the droplet concentration in all selected zones except for zone 1. Changes in the geometry of droplets modify the drag force and convective heat transfer on the surface. Increasing the surface area of a droplet relative to its volume can aid increasing the rate of evaporation, and therefore, the rate of evaporation for non-spherical droplets is higher than that for spherical droplets [58,89]. When the droplet diameter falls below $200\mu m$, the geometrical variance is negligible [44]. Hence, according to Fig. 12a, the most important factor affecting evaporation rate is variation in the ventilation velocity. The contact surface of droplets with $1\mu m < d_p < 100\mu m$ and $100\mu m < d_p < 250\mu m$ differs by only 9%. Yet, this small difference can affect the evaporation rate by up to 40% at constant ambient temperature and velocity of $0.361m/s$. Further, the results imply that the droplets with diameters<60 μm hardly deposit or evaporate.

Table 3
The average deposition range and floating time for different droplets' diameters.

Droplet size	$V_{vent}(m.s^{-1})$			Suspended time (s) (95% of total)		
	$0(m.s^{-1})$	$0.1(m.s^{-1})$	$0.3(m.s^{-1})$	$0(m.s^{-1})$	$0.1(m.s^{-1})$	$0.3(m.s^{-1})$
1–5	0.214	0.457	0.663	600	600	600
5–20	0.197	0.422	0.654	600	600	600
20–50	0.188	0.403	0.636	587	600	600
50–100	0.176	0.395	0.611	552	598	600
100–150	0.162	0.364	0.574	501	547	578
150–250	0.145	0.299	0.522	474	501	544

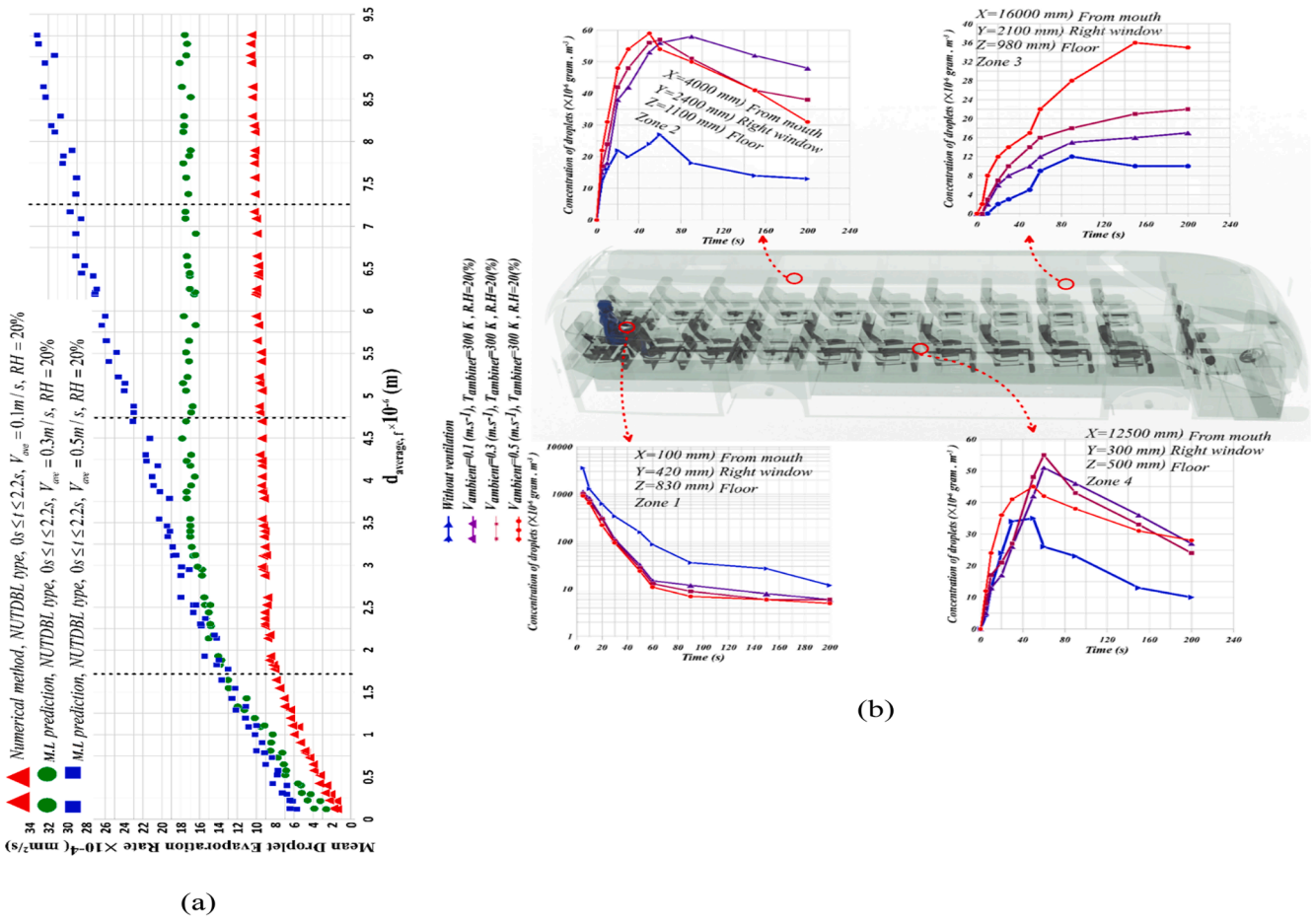

Fig. 11. a) Variation of evaporation rate with different V_{vent}, b) Variation in the concentration of droplets ($1\mu m < d_p < 250\mu m$) at various locations over time. Boundary condition for no ventilation is based on Ref. [10].

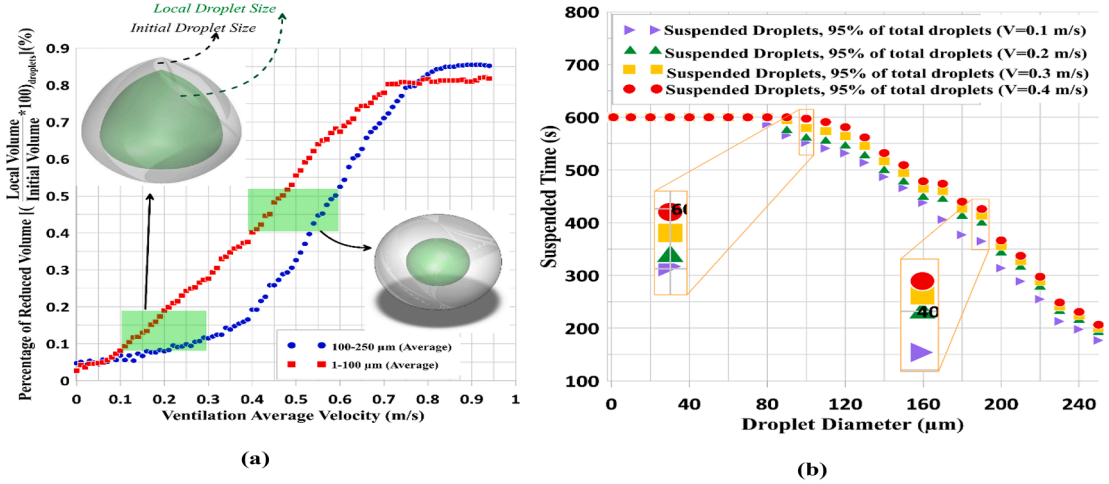

Fig. 12. a) Percentage of reduced droplets against V_{vent} for $1\mu m < d_p < 100\mu m$ and $100\mu m < d_p < 250\mu m$ $T_{vent} = 298.15K$, RH = 20%, ML predictions b) Suspension time against droplet diameter, $T_{vent} = 298.15K$, RH = 20%, ML predictions.

5.4. Humidity

Ambient humidity can affect the transmittance of contaminated droplets for a variety of reasons. Droplet evaporation is heavily influenced by humidity. Increased humidity reduces evaporation by reducing the difference in vapour concentration between the fluid and gas phases. This has the potential to increase the lifetime of the droplet and subsequently extend its transmission range. The changes in evaporation as a function of the mean diameter of the droplet are depicted in Fig. 13 for various relative humidity values. Reduced humidity increases the evaporation rate. By decreasing the concentration gradient around the droplets, the average rate of evaporation drops and therefore increases in humidity reduce the evaporation rate. Further, there is a relationship between the ambient temperature and relative humidity that affects the

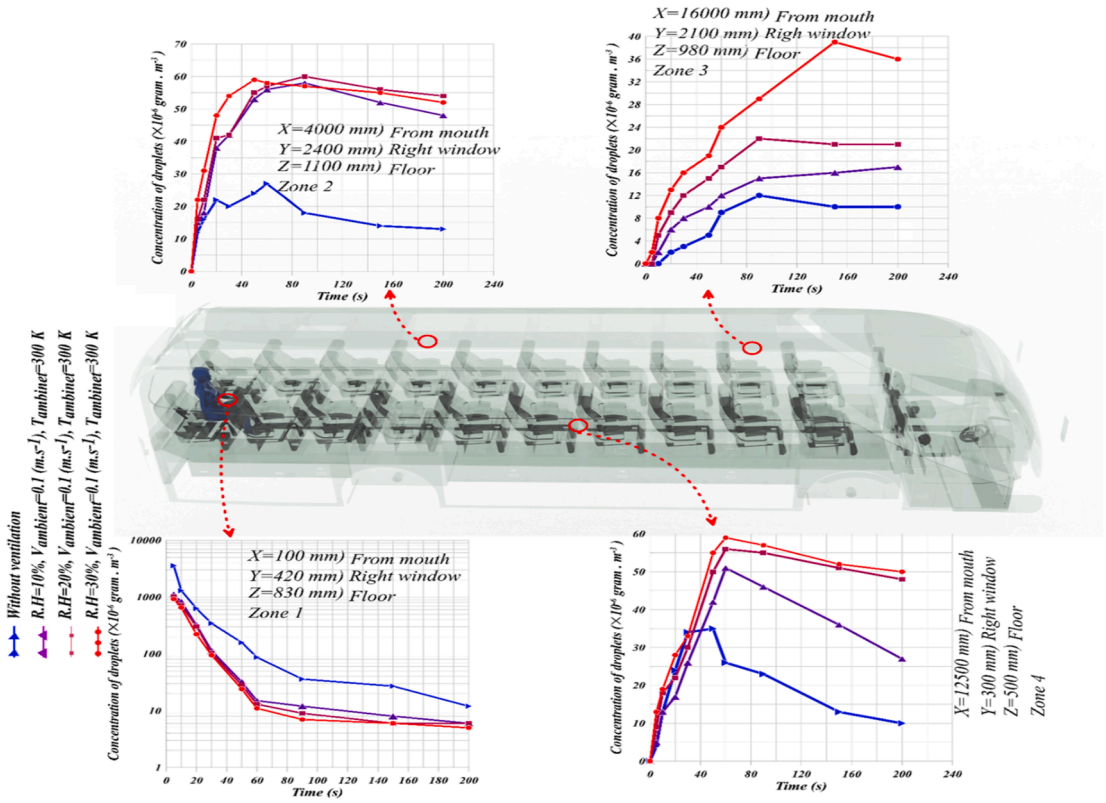

Fig. 13. Variation of droplet geometry (surface) and evaporation rate based on droplet surface for 2 s, $T_{vent} = 298.15K$, $V_{vent} = 0.1m.s^{-1}$. Boundary condition for no ventilation is based on Ref. [10].

Table 4
Thermal comfort recommendations based on ML predictions in comparison to ASHRAE standard and optimal bus conditions with a minimum concentration of droplets.

	$Temperature(K)$	$V_{vent}(m.s^{-1})$	$Humidity(\%)$
Thermal comfort (ASHRE)	$291.483 < T < 295.372$	$0.9 < V < 1.1$	$30 < R.H < 60$
Proposed to reduce droplet dispersion (M.L. predictions)	$291.15 < T < 292.240$	$0.3 < V < 0.41$	$15 < R.H < 30$
Average concentration in the bus ratio (%) ($1\mu m < d_p < 250\mu m$)	−12.36 *−13.62 (total)*	−19.47	−10.55

vapour concentration. These two factors are responsible for the reduction in the mass of droplets.

Fig. 13 illustrates the evaporation rate as a function of variations in the droplet surface, showing that by raising the humidity (averaged for the entire bus) by 20%, the average evaporation decreases up to 50%. Fig. 13 demonstrates the effects on the droplet concentrations as a function of humidity. This suggests that increasing humidity may aid the growth of droplets' concentration in the far-field. As illustrated in Fig. 13, if ventilation is controlled to maintain an optimal humidity level (Table 4), the concentration of droplets can be significantly reduced. The optimal thermal comfort (as defined by ASHRAE standard 55) is shown in Table 4 when the droplets concentration is minimised.

According to Table 4, the optimal combination of humidity, temperature, and velocity can reduce the concentration of droplets (1md p250m) by 13.62% when compared to the ASHRAE standard condition.

6. Conclusions

A hybridised CFD/ML predictive tool was used to analyse the distribution of virus-containing droplets generated by human sneezing in public transport (a bus). The tool was rigorously validated and then utilised to explore the influence of environmental parameters including temperature, relative humidity and ventilation on the Spatio-temporal distribution of the droplets. In particular, emphasis was put on the droplets suspension time and transmission speed through the interior space of the bus. An earlier study of the authors showed that the droplets with diameters below $250\mu m$ are most responsible for virus transmission. Hence, this investigation focused on the droplets with diameters between 1 and 250 μm. The key findings of this work could be summarised as follows.

- When the ventilation system of the bus is switched off, the droplets ($1 \sim 250\mu m$) take more than 200 s to reach the front end of the bus. However, with the ventilation system running, this time drops to 22 s for $V_{vent} = 0.1m.s^{-1}$, 15 s for $V_{vent} = 0.3m.s^{-1}$, and 1.8 s for $V_{vent} = 0.5m.s^{-1}$. Therefore, in general, ventilation could accelerate transmission of the virus under certain circummecetances.
- It was found that the droplets with diameters between 1 and 20 μm remain suspended in the air without deposition or evaporation for an extended period of time.
- Environmental parameters can have significant effects on the concentration of the droplets with diameters between 1 and $250\mu m$. For instance, increasing the relative humidity by 10% can result in 30%

increase in the droplet concentration at the farthest distance from a sneezing passenger.
- Configuration of the ventilation system design can aid or hinder dispersion of small infectious droplets. According to the results, the optimal ventilation system can be designed by injecting fresh air from the ceiling and sucking air from the floor.
- The results indicated that the highest thermal comfort and the lowest risk of droplet dispersion (-13.62 %) were achievable when 291.15 K $< T_{ambient} <$ 292.240 K, 0.3 m/s $< V_{vent} <$ 0.41 m/s and 15% <RH < 30%.

Finally, it is essential to note that the number of viruses contained in the droplets can affect the risk of disease trasnmission. This biological factor was not included in the current analysis and therefore generalisation of the results should be done mindfully.

CRediT authorship contribution statement

Mehrdad Mesgarpour: Conceptualization, Software, Validation, Formal analysis, Writing – review & editing, Writing – original draft. **Javad Mohebbi Najm Abad:** Software, Data curation, Investigation. **Rasool Alizadeh:** Investigation, Project administration. **Somchai Wongwises:** Resources, Supervision. **Mohammad Hossein Doranehgard:** Writing – review & editing. **Saeed Jowkar:** Writing – review & editing. **Nader Karimi:** Conceptualization, Supervision, Project administration, Writing – review & editing.

Declaration of Competing Interest

The authors declare that they have no known competing financial interests or personal relationships that could have appeared to influence the work reported in this paper.

Acknowledgement

M. Mesgarpour acknowledges Postdoctoral Fellowship from KMUTT. S. Wongwises acknowledges the support provided by the ''Research Chair Grant'' National Science and Technology Development Agency (NSTDA). N. Karimi acknowledges the financial support by the Engineering and Physical Science Research Council, UK, through the grant number EP/V036777/1 Risk Evaluation Fast Intelligent Tool (RELIANT) for COVID 19.

Appendix A:

Comparisons between CFD results and ML predictions

Appendix B. Supplementary data

Supplementary data to this article can be found online at https://doi.org/10.1016/j.cej.2021.132761.

References

[1] S. Meyer, C. Papan, K. Last, A global health perspective on SARS-CoV-2—hazards, disaster and hope, Wien. Med. Wochenschr. 170 (13) (2020) 357–358.
[2] Y. Feng, et al., Influence of wind and relative humidity on the social distancing effectiveness to prevent COVID-19 airborne transmission: A numerical study, J. Aerosol Sci. 147 (2020), 105585.
[3] R.R. Netz, W.A. Eaton, Physics of virus transmission by speaking droplets, Proc. Natl. Acad. Sci. 117 (41) (2020) 25209–25211.
[4] W.F. Wells, On air-borne infection. Study II. Droplets and droplet nuclei. Am. J. Hygiene 20 (1934) 611–618.
[5] R. Mittal, R. Ni, J.-H. Seo, The flow physics of COVID-19, J. Fluid Mech. 894 (2020).
[6] G. Busco, et al., Sneezing and asymptomatic virus transmission, Phys. Fluids 32 (7) (2020), 073309.
[7] L. Bourouiba, Turbulent gas clouds and respiratory pathogen emissions: potential implications for reducing transmission of COVID-19, JAMA 323 (18) (2020) 1837–1838.
[8] S.K. Das, et al., Transmission of airborne virus through sneezed and coughed droplets, Phys. Fluids 32 (9) (2020), 097102.
[9] S.H. Smith, et al., Aerosol persistence in relation to possible transmission of SARS-CoV-2, Phys. Fluids 32 (10) (2020), 107108.
[10] M. Mesgarpour, et al., Prediction of the spread of Corona-virus carrying droplets in a bus-A computational based artificial intelligence approach, J. Hazard. Mater. (2021), 125358.
[11] M. Jayaweera, et al., Transmission of COVID-19 virus by droplets and aerosols: A critical review on the unresolved dichotomy, Environ. Res. (2020), 109819.
[12] Z. Han, W. Weng, Q. Huang, Characterizations of particle size distribution of the droplets exhaled by sneeze, J. R. Soc. Interface 10 (88) (2013) 20130560.
[13] J. Ren, et al., Numerical study of three ventilation strategies in a prefabricated COVID-19 inpatient ward, Build. Environ. (2020), 107467.
[14] A. Khosronejad, et al., Fluid dynamics simulations show that facial masks can suppress the spread of COVID-19 in indoor environments, AIP Adv. 10 (12) (2020), 125109.
[15] M. Abuhegazy, et al., Numerical investigation of aerosol transport in a classroom with relevance to COVID-19, Phys. Fluids 32 (10) (2020), 103311.
[16] H. Li, et al., Dispersion of evaporating cough droplets in tropical outdoor environment, Phys. Fluids 32 (11) (2020), 113301.
[17] R.K. Singh, S.N. Tripathi, Application of national aerosol facility (naf) in designing of a ventilation system for isolation rooms to minimize interpersonal exposure of sneezing/coughing, Trans. Ind. Nat. Acad. Eng. (2020) 1.
[18] Chaudhuri, S., et al., Modeling ambient temperature and relative humidity sensitivity of respiratory droplets and their role in determining growth rate of covid-19 outbreaks. arXiv preprint arXiv:2004.10929, 2020.
[19] L. Christodoulou, et al., State prediction of an entropy wave advecting through a turbulent channel flow, J. Fluid Mech. 882 (2020).
[20] J.M.N. Abad, et al., Analysis of transport processes in a reacting flow of hybrid nanofluid around a bluff-body embedded in porous media using artificial neural network and particle swarm optimization, J. Mol. Liq. (2020), 113492.
[21] R. Alizadeh, et al., Application of machine learning to investigation of heat and mass transfer over a cylinder surrounded by porous media-the radial basic function network, J. Energy Res. Technol. (2020) 1–18.
[22] Y. Varol, et al., Prediction of flow fields and temperature distributions due to natural convection in a triangular enclosure using Adaptive-Network-Based Fuzzy Inference System (ANFIS) and Artificial Neural Network (ANN), Int. Commun. Heat Mass Transfer 34 (7) (2007) 887–896.
[23] S. Andalib, K. Taira, H.P. Kavehpour, Data-driven time-dependent state estimation for interfacial fluid mechanics in evaporating droplets, Sci. Rep. 11 (1) (2021) 1–11.
[24] L. Hamadeh, et al., Machine learning analysis for quantitative discrimination of dried blood droplets, Sci. Rep. 10 (1) (2020) 1–13.
[25] Y.M. Seo, et al., Direct numerical simulation and artificial neural network modeling of heat transfer characteristics on natural convection with a sinusoidal cylinder in a long rectangular enclosure, Int. J. Heat Mass Transf. 152 (2020), 119564.
[26] R. Alizadeh, et al., A machine learning approach to the prediction of transport and thermodynamic processes in multiphysics systems-heat transfer in a hybrid nanofluid flow in porous media, J. Taiwan Inst. Chem. Eng. (2021).
[27] R. Alizadeh, et al., A machine learning approach to predicting the heat convection and thermodynamics of an external flow of hybrid nanofluid, J. Energy Res. Technol. 143 (7) (2021), 070902.
[28] R. Alizadeh, et al., Artificial intelligence prediction of natural convection of heat in an oscillating cavity filled by CuO nanofluid, J. Taiwan Inst. Chem. Eng. (2021).
[29] S.K. Chaudhry, S.P. Elumalai, The influence of school bus ventilation scenarios over in-cabin PM number concentration and air exchange rates, Atmos. Pollut. Res. 11 (8) (2020) 1396–1407.
[30] DENSO. Bus Air Conditioning. 2021 June 5, 2021]; Available from: https://www.denso.com.au/bus-air-conditioning.
[31] M. Hegar, et al., Bus HVAC energy consumption test method based on HVAC unit behavior, Int. J. Refrig 36 (4) (2013) 1254–1262.
[32] Mercedes-Benz. Air conditioning systems. 2021 June 5, 2021]; Available from: https://www.mercedes-benz-bus.com/en_CY/brand/omnibus-magazin/hygienic-and-safety-measures-in-times-of-corona.html.
[33] M. Mesgarpour, et al., Prediction of the spread of Corona-virus carrying droplets in a bus-A computational based artificial intelligence approach, J. Hazard. Mater. 413 (2021), 125358.
[34] M.-R. Pendar, J.C. Páscoa, Numerical modeling of the distribution of virus carrying saliva droplets during sneeze and cough, Phys. Fluids 32 (8) (2020), 083305.
[35] D. Brezgin, K. Aronson, Nozzle design influence on the steam-driven ejector. Journal of Physics: Conference Series, IOP Publishing, 2020.
[36] M. Mesgarpour, et al., A CFD Study of [C2mim][CH3SO3]/Al 2 O 3 ionanofluid flow and heat transfer in grooved tubes, Int. J. Thermophys. 42 (3) (2021) 1–17.
[37] M. Antuono, et al., The δ-ALE-SPH model: An arbitrary Lagrangian-Eulerian framework for the δ-SPH model with particle shifting technique, Comput. Fluids 216 (2021), 104806.
[38] M. Mohammadiun, et al., The effect of variable temperature and location on relative thermal conductivity (RTC) on the heat pipe in the presence of AL2O3 nanoparticles: Numerical and optimization approaches, J. Taiwan Inst. Chem. Eng. (2021).
[39] J. Ren, et al., Hydrodynamic pattern in drying saline droplet with suspended nanoparticles, J. Bionic Eng. 17 (4) (2020) 802–808.

[40] Y. Li, et al., Three-dimensional numerical simulation of violent free surface deformation based on a coupled level set and volume of fluid method, Ocean Eng. 210 (2020), 106794.
[41] Prosperetti, A. and G. Tryggvason, Computational methods for multiphase flow. 2009: Cambridge university press.
[42] Kolev, N.I. and N.I. Kolev, Multiphase flow dynamics: Fundamentals. Vol. 1. 2007: Springer.
[43] Yeoh, G.H. and J. Tu, Computational techniques for multiphase flows. 2019: Butterworth-Heinemann.
[44] Crowe, C.T., et al., Multiphase flows with droplets and particles. 2011: CRC press.
[45] Borghi, R. and F. Anselmet, Turbulent multiphase flows with heat and mass transfer. 2014: Wiley Online Library.
[46] Crowe, C.T., Multiphase flow handbook. Vol. 59. 2005: CRC press.
[47] Pope, S.B., Turbulent flows. 2001, IOP Publishing.
[48] W.D. McComb, The physics of fluid turbulence, Chem. Phys. (1990).
[49] D. König, M. Meinke, W. Schröder, Embedded LES-to-RANS boundary in zonal simulations, J. Turbul. 11 (2010) N7.
[50] L. Davidson, M. Billson, Hybrid LES-RANS using synthesized turbulent fluctuations for forcing in the interface region, Int. J. Heat Fluid Flow 27 (6) (2006) 1028–1042.
[51] S. Jakirlic, B. Kniesner, G. Kadavelil, On interface issues in LES/RANS coupling strategies: a method for turbulence forcing, J. Fluid Sci. Technol. 6 (1) (2011) 56–72.
[52] J.W. Tang, et al., Airflow dynamics of human jets: sneezing and breathing-potential sources of infectious aerosols, PLoS ONE 8 (4) (2013), e59970.
[53] E.P. Vejerano, L.C. Marr, Physico-chemical characteristics of evaporating respiratory fluid droplets, J. R. Soc. Interface 15 (139) (2018) 20170939.
[54] F. Akagi, et al., Effect of sneezing on the flow around a face shield, Phys. Fluids 32 (12) (2020), 127105.
[55] M. Almechkor, et al., Development of a Simulator to Model the Spread of Coronavirus Infection in a Closed Space, Springer, 2020.
[56] X. Niu, et al., Pillar-induced droplet merging in microfluidic circuits, Lab Chip 8 (11) (2008) 1837–1841.
[57] D. Stefanitsis, et al., Improved droplet breakup models for spray applications, Int. J. Heat Fluid Flow 76 (2019) 274–286.
[58] S. Nešić, J. Vodnik, Kinetics of droplet evaporation, Chem. Eng. Sci. 46 (2) (1991) 527–537.
[59] Michaelides, E., Particles, bubbles & drops: their motion, heat and mass transfer. 2006: World Scientific.
[60] Z.-G. Feng, E.E. Michaelides, Drag coefficients of viscous spheres at intermediate and high Reynolds numbers, J. Fluids Eng. 123 (4) (2001) 841–849.
[61] L. Sang, et al., Liquid flow pattern transition, droplet diameter and size distribution in the cavity zone of a rotating packed bed: A visual study, Chem. Eng. Sci. 158 (2017) 429–438.
[62] M. Mesgarpour, et al., The comparative investigation of three approaches to modeling the natural convection heat transfer: A case studyon conical cavity filled with Al2O3 nanoparticles, J. Taiwan Inst. Chem. Eng. (2021).
[63] Y. Bai, et al., A double droplet trap system for studying mass transport across a droplet-droplet interface, Lab Chip 10 (10) (2010) 1281–1285.
[64] K.-I. Sugioka, S. Komori, Drag and lift forces acting on a spherical water droplet in homogeneous linear shear air flow, J. Fluid Mech. 570 (2007) 155.
[65] E. Loth, Quasi-steady shape and drag of deformable bubbles and drops, Int. J. Multiph. Flow 34 (6) (2008) 523–546.
[66] Y. Suh, C. Lee, A numerical method for the calculation of drag and lift of a deformable droplet in shear flow, J. Comput. Phys. 241 (2013) 35–57.
[67] K. Bergeles, Y. Hardalupas, A. Taylor, On the transient flow inside and around a deforming millimetre class oil droplet falling under the action of gravity in stagnant air, Phys. Fluids 30 (1) (2018), 013305.
[68] D. Kincaid, T. Longley, A water droplet evaporation and temperature model, Transac. ASAE 32 (2) (1989) 457–0462.
[69] R. Ragab, T. Wang, An Investigation of Liquid Droplet Evaporation Model Used in Multiphase Flow Simulation, American Society of Mechanical Engineers, 2012.
[70] L. Dombrovsky, S. Sazhin, A simplified non-isothermal model for droplet heating and evaporation, Int. Commun. Heat Mass Transfer 30 (6) (2003) 787–796.
[71] L.A. Dombrovsky, et al., Stable cluster of identical water droplets formed under the infrared irradiation: Experimental study and theoretical modeling, Int. J. Heat Mass Transf. 161 (2020), 120255.
[72] Y. Wang, et al., Evaporation and movement of fine droplets in non-uniform temperature and humidity field, Build. Environ. 150 (2019) 75–87.
[73] H.L.-u. Rehman, J. Weiss, P. Seers, Effect of heat conduction on droplet life time and evaporation rate under forced convection at low temperatures, Exp. Therm Fluid Sci. 72 (2016) 59–66.
[74] Ivorra, B., et al., Mathematical modeling of the spread of the coronavirus disease 2019 (COVID-19) taking into account the undetected infections. The case of China. Communications in nonlinear science and numerical simulation, 2020. 88: p. 105303.
[75] G. Meccariello, O. Gallo, What ENT doctors should know about COVID-19 contagion risks, Authorea Preprints (2020).
[76] Enserink, M. and K. Kupferschmidt, With COVID-19, modeling takes on life and death importance. 2020, American Association for the Advancement of Science.
[77] S. Chaudhuri, et al., Modeling the role of respiratory droplets in Covid-19 type pandemics, Phys. Fluids 32 (6) (2020), 063309.
[78] S.S. Diwan, et al., Understanding transmission dynamics of covid-19-type infections by direct numerical simulations of cough/sneeze flows, Transact. Ind. Nat. Acad. Eng. (2020) 1.
[79] M. Rafiq, G. Bugmann, D. Easterbrook, Neural network design for engineering applications, Comput. Struct. 79 (17) (2001) 1541–1552.
[80] S.J. Alter, K.J. Weilmuenster, The three-dimensional multi-block advanced grid generation system (3DMAGGS), NASA STI/Recon Technical Report N 93 (1993) 29155.
[81] Z. Zhao, et al., A large-scale parallel hybrid grid generation technique for realistic complex geometry, Int. J. Numer. Meth. Fluids 92 (10) (2020) 1235–1255.
[82] L. Bourouiba, E. Dehandschoewercker, J.W. Bush, Violent expiratory events: on coughing and sneezing, J. Fluid Mech. 745 (2014) 537–563.
[83] L.-D. Chen, Effects of ambient temperature and humidity on droplet lifetime–a perspective of exhalation sneeze droplets with covid-19 virus transmission, Int. J. Hyg. Environ. Health (2020), 113568.
[84] D. Chirizzi, et al., SARS-CoV-2 concentrations and virus-laden aerosol size distributions in outdoor air in north and south of Italy, Environ. Int. 146 (2021), 106255.
[85] S.T. Chang, O.D. Velev, Evaporation-induced particle microseparations inside droplets floating on a chip, Langmuir 22 (4) (2006) 1459–1468.
[86] X. Xie, et al., Exhaled droplets due to talking and coughing, J. R. Soc. Interface 6 (suppl_6) (2009) S703–S714.
[87] J. Duguid, The size and the duration of air-carriage of respiratory droplets and droplet-nuclei, Epidemiol. Infect. 44 (6) (1946) 471–479.
[88] K. Rajamanickam, S. Basu, On the dynamics of vortex–droplet interactions, dispersion and breakup in a coaxial swirling flow, J. Fluid Mech. 827 (2017) 572–613.
[89] P. Hamey The evaporation of airborne droplets 1982.